Journal of Sound and Vibration 632 (2026) 119727

Contents lists available at ScienceDirect

Journal of Sound and Vibration

journal homepage: www.elsevier.com/locate/jsvi

Bandgap trade-offs in a nonlinear metamaterial beam with magnetically coupled dual-resonators

Chunbo Lan [a,*], Shuo Wang [a], Xi Chen [a], Yang Lu [a], Guobiao Hu [b,*]

[a] National Key Laboratory of Helicopter Aeromechanics, Nanjing University of Aeronautics and Astronautics, Nanjing, 210016, PR China
[b] Internet of Things Thrust, The Hong Kong University of Science and Technology (Guangzhou), Guangzhou, Guangdong 511400, China

ARTICLE INFO

Keywords:
Nonlinear dynamics
Metamaterial
Local resonance
Magnetic coupling

ABSTRACT

During the past decade, structural nonlinearities have been utilized to widen the bandgaps of locally resonant metamaterials. In this paper, a metamaterial beam incorporating nonlinearly coupled dual-beam resonators is developed. First, the mathematical model and the dipole-dipole model were established. Subsequently, static analyses were performed to examine the effect of the negative stiffness on the resonant frequencies of resonators. Numerical simulations were conducted on uncoupled, linearly coupled and nonlinearly coupled metamaterial beams. Their transmittance, bandgap properties, and dynamic responses were compared. The results demonstrate that tuning the coupling stiffness induces a bandgap trade-off between the two bandgaps. A positive coupling stiffness enhances the first bandgap at the expense of the second, whereas negative coupling stiffness exhibits the opposite effect. Meanwhile, the total bandwidth of the two bandgaps remains relatively stable despite variations in internal coupling stiffness. The influence of structural nonlinearity on bandgap performance under different excitation levels is subsequently investigated. It is found that both bandgaps exhibit excitation-dependence characteristics, with the low-frequency bandgap being more sensitive to excitation than the high-frequency one. As the base excitation increases, the bandwidth of the low-frequency bandgap gradually decreases and eventually vanishes, while the high-frequency bandgap experiences only a slight shift in its starting frequency. Both sinusoidal and random vibration experiments were conducted for validation. Experimental results show good agreement with analytical and numerical predictions. By leveraging the bandgap trade-off mechanism, the limited total bandgap can be effectively allocated to meet specific vibration attenuation requirements through tuning of the coupling stiffness, thereby enhancing the flexibility of the internally coupled locally resonant metamaterial beam.

1. Introduction

As space exploration advances, th e rapid development of satellites, space stations, and other spacecraft has led to increasingly stringent requirements for safety and stability [1]. Micro-vibrations, with their low frequency, small amplitude, and challenging control [2], impose significant constraints on satellites' pointing precision and stability. This issue is particularly critical for platforms such as remote sensing satellites, space telescopes, and laser communication systems, which require exceptional pointing accuracy and stability. Micro-vibrations can severely degrade the performance of these systems. Therefore, the development of effective

* Corresponding authors.
E-mail addresses: chunbolan@nuaa.edu.cn (C. Lan), guobiaohu@hkust-gz.edu.cn (G. Hu).

https://doi.org/10.1016/j.jsv.2026.119727
Received 17 July 2025; Received in revised form 20 December 2025; Accepted 20 February 2026
Available online 20 February 2026

low-frequency vibration suppression technologies is essential to enhancing the operational capabilities of modern satellites.

Locally resonant metamaterials, known for their superior performance in suppressing low-frequency vibrations, have rapidly developed and found widespread applications since their inception [3]. Compared to Bragg scattering (BS) bandgaps, locally resonant (LR) ones are more effective for sub-wavelength low-frequency vibration suppression. However, LR bandgaps are typically narrow, and a decrease in the frequency of the local resonators, while keeping the parasitic mass constant, leads to a rapid reduction in the bandgap width [4]. According to the classical linear theory, widening the low-frequency bandgap requires increasing the parasitic mass, provided that static load capacity is not compromised. This presents significant challenges in fields such as aerospace engineering, where stringent mass constraints and a preference for lightweight solutions are key considerations [5].

Numerous efforts have been devoted to developing innovative metamaterials to widen low-frequency LR bandgaps. Among the proposed solutions are the incorporation of multi-degree-of-freedom (MDOF)/array local resonators [6–12], the integration of nonlinearities [13–29], and the introduction of internally coupled mechanisms [30–34]. MDOF solutions refer to replacing original SDOF oscillators with MDOF ones, thereby generating multiple LR bandgaps. For example, Huang et al. [6] proposed a metamaterial integrated with 2DOF oscillators, resulting in the creation of an additional bandgap. Hu et al. [7] developed a gradient LR metamaterial by varying the resonant frequencies of adjacent oscillators. Their results demonstrated that this method could increase the low-frequency bandgap width by up to 150 %. Miao et al. [8] proposed a composite cylindrical LR metamaterial plate. The results show that compared with the original periodic metamaterial plate, the non-periodic gradient design widens the bandgap by 67.9 % and achieves better vibration suppression performance within the target frequency range. Yi et al. [9] proposed an LR metamaterial sheet structure and established a compound band structure calculation model containing aggregated total resonant elements using the plane wave expansion method. The results show that the bandgaps can be significantly broadened by regulating the natural frequency of the resonators. When tuned to a specific value, the two bandgaps are coupled to form an ultra-wide pseudo-directional bandgap (including only an extremely narrow passband), which effectively broadens the low-frequency bandgap. Jian et al. [10] used piezoelectric cantilever beams as oscillators to construct a gradient metamaterial beam and achieved a similar improvement in widening bandgaps. Yi et al. [11] proposed a general method for designing multi-resonant piezoelectric metamaterials by constructing a generalized transfer function to regulate the equivalent bending stiffness, enabling it to exhibit negative values across multiple frequency ranges and thereby generating multiple bandgaps to broaden the low-frequency vibration damping bandwidth. It was found that gradient LR metamaterials present a trade-off: while the bandgap is significantly broadened, the vibration suppression performance within the bandgap becomes weakened.

As the name suggests, nonlinear LR metamaterials utilize nonlinear oscillators, such as Duffing oscillators, to create local resonance. By leveraging the broadband frequency response characteristics of the nonlinear oscillator, broadband vibration suppression can be effectively achieved. Fang et al. [13] demonstrated a strongly nonlinear LR metamaterial. Experimental results showed that the nonlinear bandgap varied with the external excitation, and this nonlinearity could transform the traditional passband into a chaotic band, thereby significantly widening the vibration suppression frequency range. Chen et al. [14] derived the approximate dispersion relation of nonlinear LR metamaterials with Duffing oscillators and found that nonlinear soft stiffness is beneficial to widening the LR bandgap. Wu et al. [15] proposed a nonlinear metamaterial based on X-shaped oscillators and obtained a wide bandgap within the frequency range of 150–250 Hz. Zhou et al. [16] employed negative stiffness structures as oscillators, and their results indicated that negative stiffness could effectively reduce the equivalent dynamic stiffness of the oscillators, resulting in an ultra-low frequency bandgap. Zhang et al. [17] designed a nonlinear metamaterial beam using 2DOF bistable oscillators, and their simulation results indicated that structural nonlinearity could increase the bandgap width by 35.9 %. As research progresses, various characteristics of nonlinear bandgaps [26], such as amplitude-dependence [27], subharmonic generation [28], and nonreciprocal propagation [29], have been discovered and reported. Although nonlinear metamaterials offer innovative approaches for manipulating elastic waves, their unstable performance, resulting from bifurcation and chaos, requires further improvements in robustness and reliability to ensure their practical applications in engineering.

Internally coupled LR metamaterials, a novel type of low-frequency metamaterial developed in recent years, are created by coupling adjacent oscillators through mechanisms such as springs or piezoelectric shunt circuits. By tuning the coupling strength, the low-frequency bandgap can be effectively controlled and expanded. This approach not only avoids a significant increase in the geometric size but also leverages the advantages of both linear and nonlinear metamaterials. Banerjee et al. [30] introduced a metamaterial that coupled oscillators with inertial amplification components. Theoretical results showed that the LR bandgap and the inertial amplification bandgap can merge into a single, wide one, significantly expanding the frequency range of the bandgap. Fang et al. [31] proposed a bridge-coupled nonlinear metamaterial. Due to the equivalent negative mass generated by nonlinear coupled oscillators, a chaotic band between two LR bandgaps was produced, thereby substantially widening the vibration suppression frequency range. Hu et al. [32] conducted theoretical and simulation studies on linearly coupled chain-type metamaterials. Results showed that an additional bandgap is generated due to internal coupling. Hu et al. [33] then further proposed an internally coupled metamaterial that incorporates negative stiffness springs. Theoretical results showed that coupling springs with negative stiffnesses could effectively shift two LR bandgaps to ultra-low frequencies, which was validated by Xue et al. [34], who used magnetic interactions to generate the negative stiffness. However, the advantages of introducing nonlinear internal coupling go far beyond bandgap reduction. To fully harness its potential, it is crucial to understand the mechanism by which it tunes low-frequency bandgaps and its ability to enlarge them. To achieve this, it is necessary to first design a tunable nonlinearly coupled metamaterial and investigate the formation and evolution of nonlinear bandgaps.

This paper proposes an adjustable nonlinear metamaterial with magnetically coupled dual-beam oscillators. Theoretical analyses, numerical simulations, and experimental tests are conducted to unveil the mechanisms behind nonlinear bandgap formation and widening. The rest of this paper is structured as follows: Section 2 presents the theoretical model of the proposed nonlinear

metamaterial; Section 3 presents a static analysis in terms of the magnetic force and resonant frequency shift; Section 4 investigates the transmittance and bandgaps of three different configurations, including an uncoupled configuration, a linearly coupled configuration, and a nonlinearly coupled configuration; experimental test results for validation are presented in Section 5, and Section 6 follows with key conclusions.

2. Theoretical model

2.1. Overview of the structure

Fig. 1 illustrates the prototype of the proposed metamaterial beam with nonlinearly coupled dual-beam oscillators. The main structure is a uniform beam, while the nonlinear coupled dual-beam oscillators are a pair of parasitic beams, each with a tip mass at its free end. The two parasitic beams are made of stainless steel and have identical height and length. To obtain two LR bandgaps, the tip masses are designed with different values. The beam with the larger mass is designated as Beam A, while the other one is labeled as Beam B. Each cantilever beam contains a permanent magnet embedded inside the tip mass. The two magnets, positioned with identical magnetic poles facing each other, generate repulsive forces. By adjusting the distance between the two magnets, the degree of nonlinearity can be controlled. When the distance is tuned sufficiently large, the metamaterial degrades to a linear one with two bandgaps produced near the resonant frequencies of the two parasite beams. As the distance is significantly reduced, strong coupling between the two beams is established, and the metamaterial exhibits pronounced nonlinearity. The main objectives of this work are to investigate how the nonlinear coupling affects bandgaps and to explore how this nonlinear coupling can be leveraged to enhance vibration attenuation performance.

2.2. Mathematical modeling

A finite long model of the proposed nonlinear metamaterial beam is depicted in Fig. 2. The host plain beam is of length L and can be divided into S unit cells. A total of $2S$ resonators, consisting of S resonator A and S resonator B, are periodically mounted along the host beam. Resonator A and resonator B are the equivalent lumped parameter models of Beam A and Beam B. The parameters m_1, m_2, k_1, k_2, c_1, and c_2 correspond to the masses, stiffnesses, and damping coefficients of resonator A and resonator B. The two resonators interact through a nonlinear spring with a stiffness of k_n, which arises from the magnetic coupling between the two parasitic beams shown in Fig. 1. The distance between the two resonators in one cell is d_1, and the distance between two resonators in adjacent cells is d_2, with the relationship $L/S = d_1 + d_2$. Notably, d_2 should be sufficiently large to ensure that the magnetic coupling between neighboring cells is negligible. The host beam with its left end clamped on a base experiences a harmonic excitation $w_b(t) = W_b e^{i\omega t}$. Correspondingly, the base acceleration amplitude is $a_{cc} = -\omega^2 W_b$.

2.2.1. Host beam

Based on the Euler-Bernoulli beam theory, the governing equation of the host beam can be written as

$$EI\frac{\partial^4 w_{rel}(x,t)}{\partial x^4} + c_s I\frac{\partial^5 w_{rel}(x,t)}{\partial x^4 \partial t} + \rho A_{cs}\frac{\partial^2 w_{rel}(x,t)}{\partial t^2} = \rho A_{cs} a_{cc} e^{iwt} - \sum_{j=1}^{S}\left[F_j^A \delta\left(x - x_j^A\right) + F_j^B \delta\left(x - x_j^B\right)\right] e^{i\omega t} \tag{1}$$

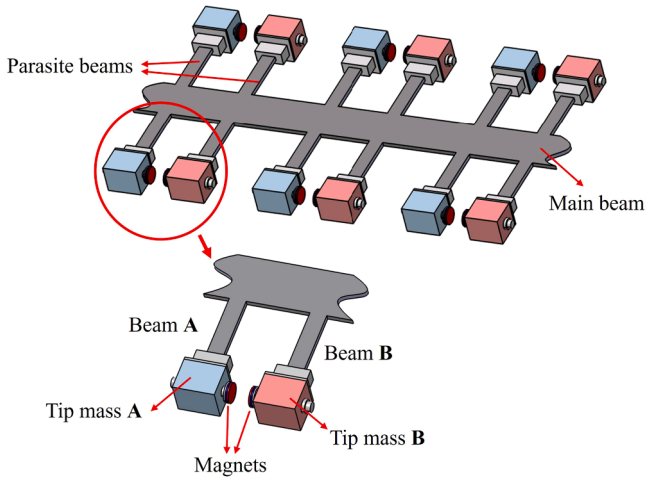

Fig. 1. Prototype of a nonlinear metamaterial beam with magnetically coupled local resonators.

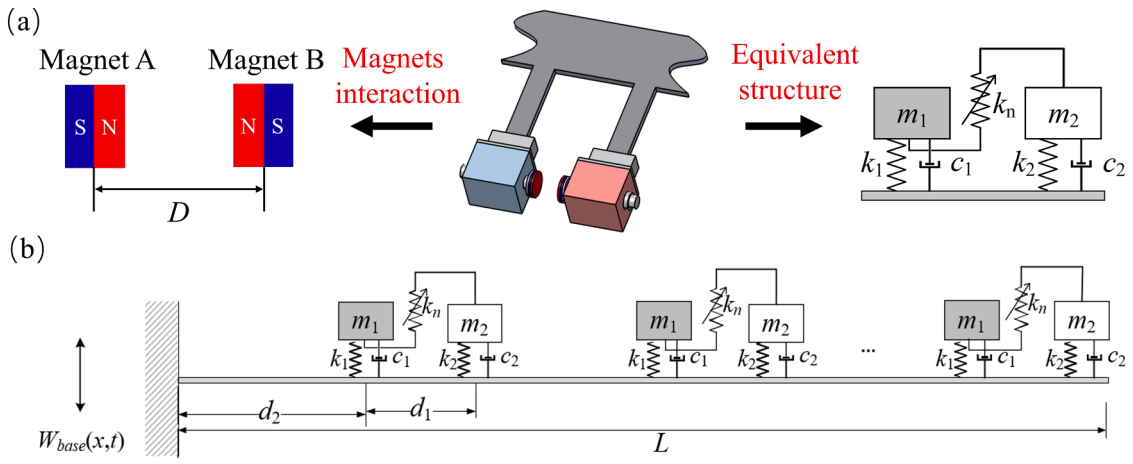

Fig. 2. Finite long model of a metamaterial beam with nonlinear coupled local resonators.

where EI, ρ, and A_{cs} are the bending stiffness, density, and cross-section area of the host beam, respectively. $w(x,t)$ is the absolute displacement of the host beam at x. $w_{rel}(x,t) = w(x,t)\text{-}w_b(t)$ is the host beam's displacement relative to the base; c_s is the equivalent strain rate damping constant; $F_j^A$and F_j^B are the reaction forces exerted by resonator A and resonator B in the jth cell onto the beam, respectively; $\delta(x)$ is the Dirac delta function.

By employing the Galerkin method, the relative displacement of the host beam $w_{rel}(x,t)$ can be written as:

$$w_{rel}(x,t) = \sum_{k=1}^{\infty} \phi_k(x)\eta_k(t)(k=1,2,3\ldots) \tag{2}$$

where $\phi_k(x)$ is the normalized host beam's mode shape function and $\eta_k(t)$ is the modal coordinate.

Substituting Eq.(2) into Eq.(1), multiplying by $\phi_n(x)$, integrating over the beam length from 0 to L, and using the orthogonal conditions, one obtains the modal governing equation:

$$\ddot{\eta}_n(t) + 2\zeta_n\omega_n\dot{\eta}_n(t) + \omega_n^2\eta_n(t) = \rho A_{cs}a_{cc}e^{i\omega t}\int_0^L \phi_n(x)dx - \sum_{j=1}^{S}\left[F_j^A\phi_n\left(x_j^A\right)e^{i\omega t} + F_j^B\phi_n\left(x_j^B\right)e^{i\omega t}\right] \tag{3}$$

where $\zeta_n = c_sI\omega_n/(2E)$.

By solving Eq.(3), the modal coordinates η_n(t) can be obtained. Substituting the coordinates back into Eq.(2), the host beam's deflection can be obtained as

$$w_{rel}(x,t) = \sum_{k=1}^{\infty}\phi_k(x)\frac{\rho A_{cs}a_{cc}\int_0^L\phi_k(x)dx - \sum_{j=1}^{S}\left[F_j^A\phi_k\left(x_j^A\right) + F_j^B\phi_k\left(x_j^B\right)\right]}{\omega_k^2 - \omega^2 + 2i\zeta_k\omega_k\omega}e^{i\omega t} \tag{4}$$

The reaction forces produced by resonator A and resonator B can be represented by:

$$\begin{cases} F_j^A = -\left[c_1\dot{u}_j^A(t) + k_1u_j^A(t)\right] \\ F_j^B = -\left[c_2\dot{u}_j^B(t) + k_2u_j^B(t)\right] \end{cases} \tag{5}$$

where $u_j^A(t)$ and $u_j^B(t)$ are the displacements of resonator A and resonator B relative to the host beam in the j^{th} cell, respectively. The overdot denotes the first derivative with respect to t.

2.2.2. Local resonators

To obtain the response of the resonators, the governing equations of resonator A and resonator B in the jth cell are given as:

$$\begin{cases} m_1\ddot{u}_j^A(t) + c_1\dot{u}_j^A(t) + k_1u_j^A(t) + F_j^{mA} = -m_1\ddot{w}\left(x_j^A,t\right) \\ m_2\ddot{u}_j^B(t) + c_2\dot{u}_j^B(t) + k_2u_j^B(t) + F_j^{mB} = -m_2\ddot{w}\left(x_j^B,t\right) \end{cases} \tag{6}$$

where F_j^{mA} and $F_j^{mB}$are the magnetic forces acting on them.

To calculate the magnetic forces, the absolute displacements of resonators A and B are used:

$$\begin{cases} U_j^A(t) = w\left(x_j^A, t\right) + u_j^A(t) \\ U_j^B(t) = w\left(x_j^B, t\right) + u_j^B(t) \end{cases} \tag{7}$$

Substituting Eq.(7) back into Eq.(6) yields:

$$\begin{cases} m_1 \ddot{U}_j^A(t) + c_1 \dot{U}_j^A(t) - c_1 \dot{w}\left(x_j^A, t\right) + k_1 U_j^A(t) - k_1 w\left(x_j^A, t\right) + F_j^{mA} = 0 \\ m_2 \ddot{U}_j^B(t) + c_2 \dot{U}_j^B(t) - c_2 \dot{w}\left(x_j^B, t\right) + k_2 U_j^B(t) - k_2 w\left(x_j^B, t\right) + F_j^{mB} = 0 \end{cases} \tag{8}$$

Subsequently, the dipole-dipole model [35] is utilized to calculate the repulsive magnetic force between resonator A and resonator B. Based on the dipole-dipole model, the potential energy between magnet A and magnet B can be written as:

$$U_m = -\frac{\mu_0}{4\pi}\left(\nabla \frac{\boldsymbol{m_B} \cdot \boldsymbol{r_{BA}}}{\| \boldsymbol{r_{BA}} \|_2^3}\right) \cdot \boldsymbol{m_A} = \frac{\mu_0}{4\pi}\left[\frac{1}{\| \boldsymbol{r_{BA}} \|_2^3}\boldsymbol{m_B} - \frac{3(\boldsymbol{m_B} \cdot \boldsymbol{r_{BA}})}{\| \boldsymbol{r_{BA}} \|_2^5}\boldsymbol{r_{BA}}\right] \cdot \boldsymbol{m_A} \tag{9}$$

where μ_0 is the vacuum permeability, $\boldsymbol{r_{BA}}$ denotes the vector from the center of magnet A to the center of magnet B, ∇ is the vector gradient operator, $\| \ \|_2$ represents the L2-norm; $\boldsymbol{m_A}$and $\boldsymbol{m_B}$ are the magnetic moment vectors of magnets A and B, respectively.

For permanent magnets, the magnitude of the magnetization vector can be evaluated using magnet's residual flux density B_r, that is, $\overline{m} = B_r/\mu_0$. Therefore, the magnetization vector of magnets A and B can be expressed as:

$$\boldsymbol{m_A} = \begin{pmatrix} \overline{m}_A \overline{v}_A \\ 0 \end{pmatrix}; \boldsymbol{m_B} = \begin{pmatrix} -\overline{m}_B \overline{v}_B \\ 0 \end{pmatrix}; \boldsymbol{r_{BA}} = \begin{pmatrix} D \\ \Delta x \end{pmatrix} \tag{10}$$

where $\overline{m}_A$ and $\overline{m}_B$ are the magnitudes of magnetization vectors, $\overline{v}_A$ and $\overline{v}_B$are the volumes of magnets, D is the horizontal distance between the two magnets' centers, $\Delta x = U_j^A(t) - U_j^B(t)$ is the vertical distance between the two magnets.

Substituting Eq.(10) into Eq.(9), we have

$$U_m\left[U_j^A(t), U_j^B(t)\right] = -\frac{\overline{m}_A \overline{m}_B \overline{v}_A \overline{v}_B \mu_0}{4\pi}\left[\left(\Delta x^2 + D^2\right)^{-1.5} - 3D^2\left(\Delta x^2 + D^2\right)^{-2.5}\right] \tag{11}$$

Thus, the magnetic force in Eq.(6) can be evaluated as:

$$\begin{cases} F_j^{mA}\left[U_j^A(t), U_j^B(t)\right] = -\frac{\overline{m}_A \overline{m}_B \overline{v}_A \overline{v}_B \mu_0}{4\pi}\left[\frac{-3\Delta x}{\left(\Delta x^2 + D^2\right)^{2.5}} + \frac{15D^2 \Delta x}{\left(\Delta x^2 + D^2\right)^{3.5}}\right] \\ F_j^{mB}\left[U_j^A(t), U_j^B(t)\right] = -\frac{\overline{m}_A \overline{m}_B \overline{v}_A \overline{v}_B \mu_0}{4\pi}\left[\frac{3\Delta x}{\left(\Delta x^2 + D^2\right)^{2.5}} - \frac{15D^2 \Delta x}{\left(\Delta x^2 + D^2\right)^{3.5}}\right] \end{cases} \tag{12}$$

Notably, since the metamaterial beam is vertically excited, the longitudinal response of the two magnets within the same unit cell is minimal; thus, the horizontal force between the coupled magnets can be neglected.

Substituting Eq.(12) into Eq.(8), the governing equations of the local resonators are obtained. By solving Eqs.(3) and (4), the relative displacement of the host beam can be obtained. The transmittance of the host beam is defined as:

$$T_r = 20\log\left(\frac{|w_{rel}(L) + w_b|}{|w_b|}\right) \tag{13}$$

3. Preliminary analysis

3.1. Magnetic force and equivalent stiffness

First, the magnetic force and its equivalent stiffness are studied. According to Eq.(12), the nonlinear forces acting on both resonator A and resonator B have the same magnitude but act in opposite directions. Differentiating Eq.(12) with respect to the vertical relative displacement Δx of the magnets gives the equivalent stiffness as:

$$\begin{cases} K_j^{mA}\left[U_j^A(t), U_j^B(t)\right] = -\frac{\overline{m}_A \overline{m}_B \overline{v}_A \overline{v}_B \mu_0}{4\pi}\left[\frac{12}{\left(\Delta x^2 + D^2\right)^{2.5}} - \frac{105D^2(\Delta x)^2}{\left(\Delta x^2 + D^2\right)^{4.5}}\right] \\ K_j^{mB}\left[U_j^A(t), U_j^B(t)\right] = -\frac{\overline{m}_A \overline{m}_B \overline{v}_A \overline{v}_B \mu_0}{4\pi}\left[\frac{12}{\left(\Delta x^2 + D^2\right)^{2.5}} - \frac{105D^2(\Delta x)^2}{\left(\Delta x^2 + D^2\right)^{4.5}}\right] \end{cases} \tag{14}$$

Based on Eqs.(12) and (14), the nonlinear force and equivalent stiffness are obtained. Fig. 3(a) depicts the relation between relative displacement and magnetic force when $D = 18$ mm. As Δx increases from -40 mm to -5 mm, the magnetic force gradually increases, reaching its maximum value of 0.308 N at -5 mm. As Δx increases beyond -5 mm, the magnetic force gradually decreases, reaching its minimum value of -0.308 N at 5 mm. As the displacement continues to increase, the force decreases further, exhibiting a negative

stiffness characteristic. Eventually, as Δx increases further, the magnetic force increases again; and when Δx becomes sufficiently large, the magnetic force approaches zero.

Fig. 3(b) further illustrates the equivalent stiffness. It is observed that when Δx is within the range of −5 mm to 5 mm, the nonlinear magnetic coupling exhibits typical negative stiffness characteristics, with the lowest negative stiffness of −75 N/m occurring at $\Delta x = 0$. Outside this range, the equivalent stiffness becomes positive and approaches zero as Δx increases sufficiently. For LR metamaterials, the displacement response within the bandgap is typically very small, whereas the response within the passband is relatively large. Based on these observations, it can be inferred that the bandgap and its response characteristics in the metamaterial beam will primarily be influenced by the negative stiffness of the magnetic coupling. This would cause the bandgap to shift towards lower frequencies and alter its width. In contrast, the characteristics within the passband will mainly be affected by the positive stiffness of the magnetic coupling, likely leading to an increase in the resonant frequencies within the passband and exhibiting typical nonlinear resonance behavior.

3.2. Resonance frequency shift

By comparing the stiffness parameters of the local resonator listed in Table 3 with the nonlinear negative stiffness observed in Fig. 3, it is evident that the negative stiffness induced by the nonlinear magnetic force will significantly influence the resonant frequency of the local resonator, thereby affecting the LR bandgap. Hence, it is essential to conduct a theoretical analysis to approximate the impact of the nonlinear magnetic force on the resonant frequency of the local resonator.

Expanding Eq.(12) in a Taylor series at $\Delta x = 0$ and neglecting higher-order terms, the magnetic force can be approximated by

$$F_j^m = \pm\frac{\overline{m}_A\overline{m}_B\overline{v}_A\overline{v}_B\mu_0}{4\pi}\left[\frac{12}{D^5}\Delta x - \frac{45}{D^7}(\Delta x)^3\right] \tag{15}$$

where "+"and "–" indicate that the magnetic force acting on beam A and beam B are opposite.

Assuming the linear part of the nonlinear stiffness as:

$$k_n = -\frac{12\overline{m}_A\overline{m}_B\overline{v}_A\overline{v}_B\mu_0}{4\pi D^5} \tag{16}$$

Subsequently, the linearized governing equation of the system Eq.(8), with the absolute displacement of the host beam $w(x, t)$ and high-order terms of the magnetic force neglected, is obtained as:

$$\begin{cases} m_1\ddot{U}_j^A(t) + c_1\dot{U}_j^A(t) + k_1U_j^A(t) + k_n\Delta x = 0 \\ m_2\ddot{U}_j^B(t) + c_2\dot{U}_j^B(t) + k_2U_j^B(t) - k_n\Delta x = 0 \end{cases} \tag{17}$$

Rewriting Eq.(17) into the matrix form, we have

$$\boldsymbol{M}\ddot{\boldsymbol{U}} + \boldsymbol{C}\dot{\boldsymbol{U}} + \boldsymbol{K}\boldsymbol{U} = 0 \tag{18}$$

where

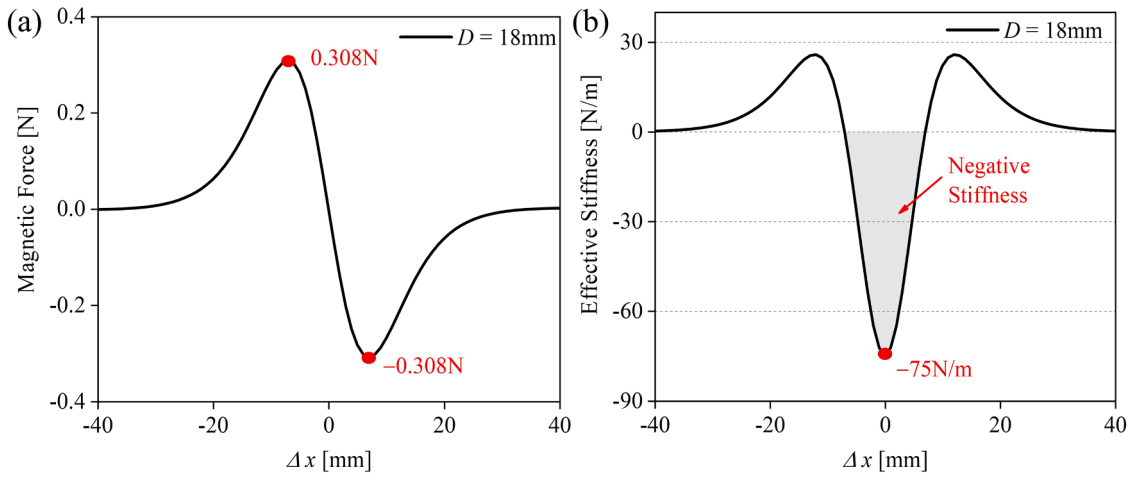

Fig. 3. Static analysis of magnetic interactions (D = 18 mm): (a) magnetic force, (b) equivalent stiffness.

$$\boldsymbol{M}=\begin{bmatrix} m_1 & 0 \\ 0 & m_2 \end{bmatrix}, \boldsymbol{C}=\begin{bmatrix} c_1 & 0 \\ 0 & c_2 \end{bmatrix}, \boldsymbol{K}=\begin{bmatrix} k_1-k_n & k_n \\ k_n & k_2-k_n \end{bmatrix}, \boldsymbol{U}=\begin{bmatrix} U_j^A(t) \\ U_j^B(t) \end{bmatrix}$$

Assuming the displacement response is

$$\boldsymbol{U}=\boldsymbol{\Phi}e^{st} \tag{19}$$

where $\boldsymbol{\Phi}$ is the modal shape vector, s is the complex frequency ($s=i\omega$).

Submitting Eq. (19) into Eq. (18), we have

$$\left(s^2\boldsymbol{M}+s\boldsymbol{C}+\boldsymbol{K}\right)\boldsymbol{\Phi}=0 \tag{20}$$

Since the mode shape vector $\boldsymbol{\Phi}$ admits a non-trivial solution, the determinant of the coefficient matrix should be zero, i.e.,

$$\left|s^2\boldsymbol{M}+s\boldsymbol{C}+\boldsymbol{K}\right|=0 \tag{21}$$

Substituting ***M, C*** and ***K*** into Eq.(21) gives

$$\begin{vmatrix} s^2m_1+sc_1+(k_1-k_n) & k_n \\ k_n & s^2m_2+sc_2+(k_2-k_n) \end{vmatrix}=0 \tag{22}$$

Simplifying Eq.(22) yields

$$\begin{aligned} &m_1m_2s^4+(m_1c_2+m_2c_1)s^3+[k_1m_2+k_2m_1-k_n(m_1+m_2)+c_1c_2]s^2 \\ &+[c_1(k_2-k_n)+c_2(k_1-k_n)]s+\left[(k_1-k_n)(k_2-k_n)-k_n^2\right]=0 \end{aligned} \tag{23}$$

By solving Eq. (23), the resonance frequencies of the nonlinear coupled dual resonators can be obtained.

To study the effect of magnetic coupling on the resonance frequencies, Fig. 4 illustrates the effect of the magnet distance D on the first two resonant frequencies of the undamped oscillators. When the magnetic distance is large (e.g., $D=30$ mm), both the magnetic force and equivalent stiffness are minimal, resulting in resonant frequencies that are nearly identical to those of its linear counterpart. As the magnetic distance decreases from 30 mm to 17 mm, the magnetic force increases rapidly, leading to a decrease in the resonant frequencies. Notably, the decrease in the fundamental natural frequency is much more pronounced than that of the second-order natural frequency. When the magnetic distance approaches 17 mm, the fundamental natural frequency approaches zero. Further reducing the distance will make the monostable system bistable. At this point, the fundamental resonant frequency begins to rise again, while the second-order natural frequency keeps decreasing. The two natural frequencies intersect at $D=14.2$ mm. Once the system becomes bistable, the dynamic and response characteristics become complex, which is beyond the scope of this paper. This study primarily focuses on the bandgap characteristics of the system in the monostable state.

Fig. 4 further presents the resonance frequencies of the damped configuration ($c_{s1}=0.9165$ N·m/s, $c_{s2}=0.5844$ N·m/s). It is observed that after introducing damping, the variation trends of the first- and second-order resonant frequencies remain consistent with those of the undamped system. The main differences are that both the first- and second-order resonant frequencies of the damped system are lower than those of the undamped system, and the intersection point of the two resonance frequencies shifts from $D=14.2$ mm to $D=13.2$ mm. In general, based on the influence of the nonlinear magnetic force on the system's resonance frequencies, it can be

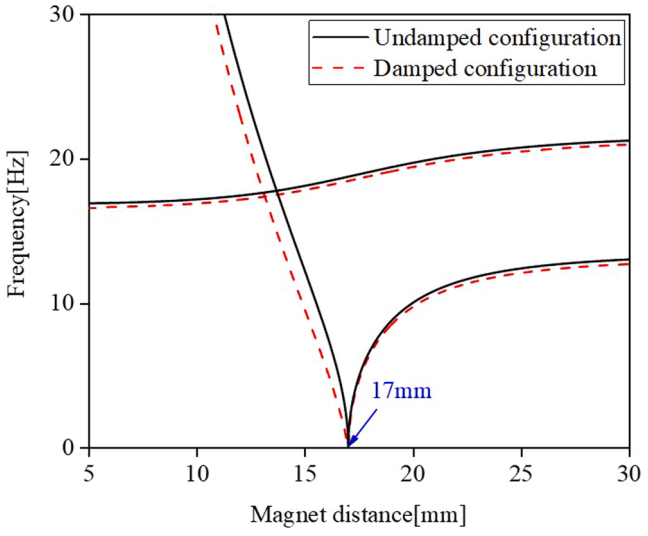

Fig. 4. Effect of magnet distance on the resonant frequencies of the magnetically coupled dual resonators.

predicted that in the monostable state, as the magnetic force increases, the first bandgap rapidly shifts toward lower frequencies, while the second bandgap gradually moves in the same direction. However, the bandwidths and response characteristics of both bandgaps require further investigation through numerical simulations.

4. Transmittance analysis

To study the bandgap and vibration suppression performance, numerical simulations are conducted to obtain the transmittance responses. Three different configurations are considered: an uncoupled metamaterial beam, a linearly coupled metamaterial beam, and a nonlinearly coupled metamaterial beam. Analytical solutions are derived for the linear configurations using the Laplace Transform method. The Runge-Kutta method is employed to numerically simulate the dynamic responses of the nonlinear configuration. Frequency linear sweep simulations are performed at a rate of 0.01 Hz/s to determine the transmittance. The parameters used in the simulations are identified from experimental tests and are listed in Table 3.

4.1. Linear uncoupled configuration

First, the uncoupled linear metamaterial beam was simulated and analyzed. Fig. 5(a) shows the model of the uncoupled linear metamaterial beam, where each unit contains two oscillators, designated as resonator A and resonator B, with distinct resonant frequencies of 13.50 Hz and 21.72 Hz, respectively. According to the theory of LR metamaterial beams, this configuration produces two local resonant bandgaps near the resonant frequencies of resonators A and B. Fig. 5(b) presents the transmittance under a base excitation of 0.1 m/s^2. Two LR bandgaps are identified within the frequency ranges of 13.35–17.40 Hz (bandgap A) and 21.06–44.67 Hz (bandgap B). The bandwidths of bandgap A and B are 4.05 Hz and 23.61 Hz, respectively. In bandgap A, the structural transmittance varies between −45 dB and −75 dB, while in bandgap B, it ranges from −58 dB to −113 dB. Both bandgaps demonstrate effective vibration suppression.

To understand how these two types of resonators affect bandgap A and bandgap B, we simulated the response distributions of the resonators along the beam at four different frequencies: P1, P2, P3, and P4, corresponding to 12.6 Hz, 15.0 Hz, 19.6 Hz, and 22.4 Hz, respectively. P1 and P3 fall within the passbands, while P2 and P4 are inside the bandgaps. From Fig. 5(c), it is clear that at P1 and P3, both the resonators and the beam exhibit strong responses. However, at P2 and P4, the responses of both resonators and the beam are significantly suppressed. The key difference between the two bandgaps lies in the roles of the two resonators. At P2 (within bandgap A), resonator A shows a much stronger response than resonator B. In contrast, at P4 (within bandgap B), resonator A exhibits a much weaker response than resonator B. In other words, resonator A primarily contributes to the formation of bandgap A, while resonator B plays a dominant role in creating bandgap B.

To summarize, although the metamaterial beam has two distinct bandgaps, only half of the resonators contribute to the formation

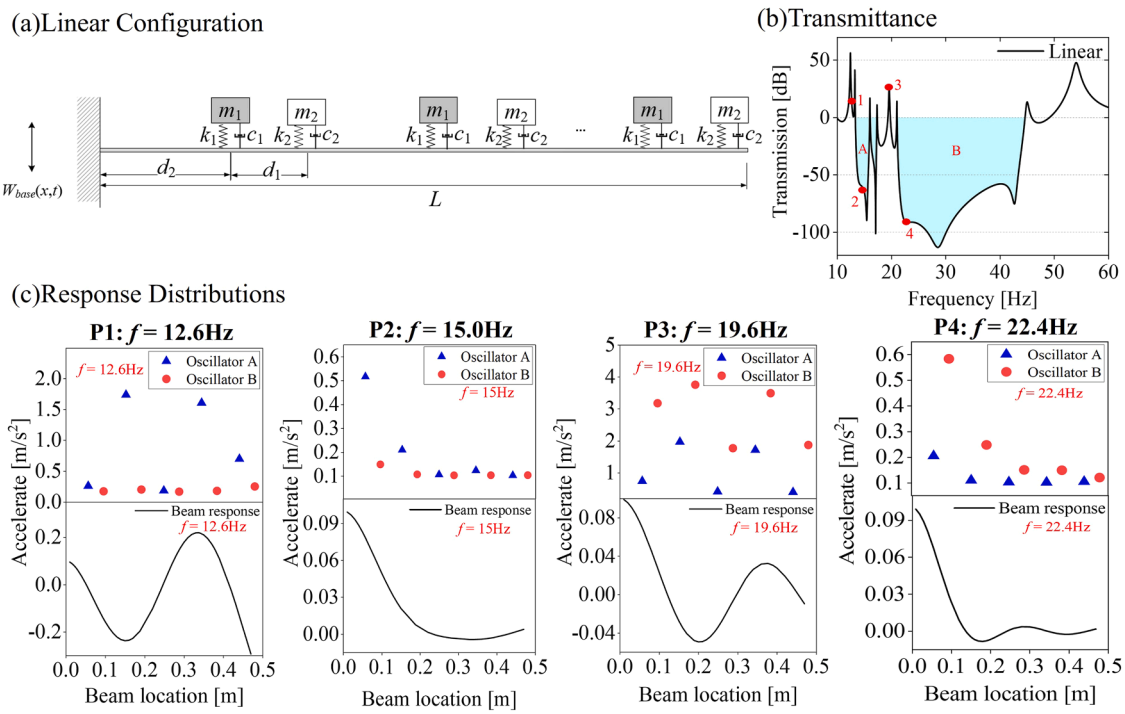

Fig. 5. Uncoupled linear metamaterial beam: (a) equivalent model, (b) transmittance, (c) response distributions at different frequencies.

of each. This suggests room for improvement by engaging all the resonators in the formation of the bandgaps.

4.2. Linearly coupled configuration

To fully utilize all the resonators, a linearly coupled metamaterial beam is constructed by introducing coupling stiffness between adjacent resonators, as illustrated in Fig. 6(a). We first investigated how the coupling stiffness affects the transmittance and bandgap. As shown in Fig. 6(b), when the coupling stiffness reduced from positive to negative values, significant changes occur in the transmittance of the entire system.

As the coupling stiffness increases from 0 N/m to 200 N/m, bandgap A widens rapidly, with both its starting and cut-off frequencies shifting to higher values. More specifically, the bandgap expands from [13.35, 17.40] Hz to [15.30, 28.00] Hz, with its bandwidth growing from 4.05 Hz to 12.70 Hz (an increase of 8.65 Hz). In the meantime, bandgap B narrows significantly, with its range shrinking from [21.06, 44.67] Hz to [31.00, 44.67] Hz, and its bandwidth reducing from 23.61 Hz to 13.67 Hz (a decrease of 9.94 Hz).

For instance, at $k_c = 50$ N/m, as depicted in Fig. 6(c), both the starting and cut-off frequencies of bandgap A (13.35 Hz and 17.40 Hz) shift to higher frequencies (14.62 Hz and 20.79 Hz). Consequently, the bandwidth of bandgap A increases from 4.05 Hz to 6.17 Hz (an increase of 2.12 Hz). However, for bandgap B, its cut-off frequency remains unchanged, while the starting frequency shifts to higher values. Thus, its bandwidth decreased from 23.61 Hz to 21.08 Hz (a decrease of 2.53 Hz). Therefore, it is known that by introducing positive stiffness to couple adjacent resonators, the bandwidth difference between these two bandgaps can be balanced and the performance of bangap A is enhanced.

For negative coupling stiffness, as the stiffness decreases from 0 N/m to −200 N/m, bandgap A rapidly narrows until it disappears, while bandgap B widens and eventually reaches a maximum. Bandgap B expands from [21.06, 44.67] Hz to [17.48, 44.67] Hz, resulting in an increase in bandwidth of 3.58 Hz. For instance, at $k_c = -50$ N/m, as shown in Fig. 6(c), bandgap A changes from [13.35, 17.40] Hz to [10.65, 12.89] Hz, with both the starting and cut-off frequencies shifting to lower values and a reduction in bandwidth of 1.81 Hz. In contrast, for bandgap B, the cut-off frequency remains unchanged, while the starting frequency shifts to lower values. Its range changes from [21.06, 44.67] Hz to [19.41, 44.67] Hz, resulting in an increase in bandwidth of 1.65 Hz. Therefore, it is evident that introducing negative stiffness promotes the performance of Bandgap B.

The physical mechanism of the bandgap trade-off phenomena can be explained as follows: By introducing an internal coupling stiffness between the two local resonators, the originally independent oscillators become mechanically coupled, forming a new two-degree-of-freedom local resonance system. The physical interpretation of bandgap trade-off lies in the energy exchange between these

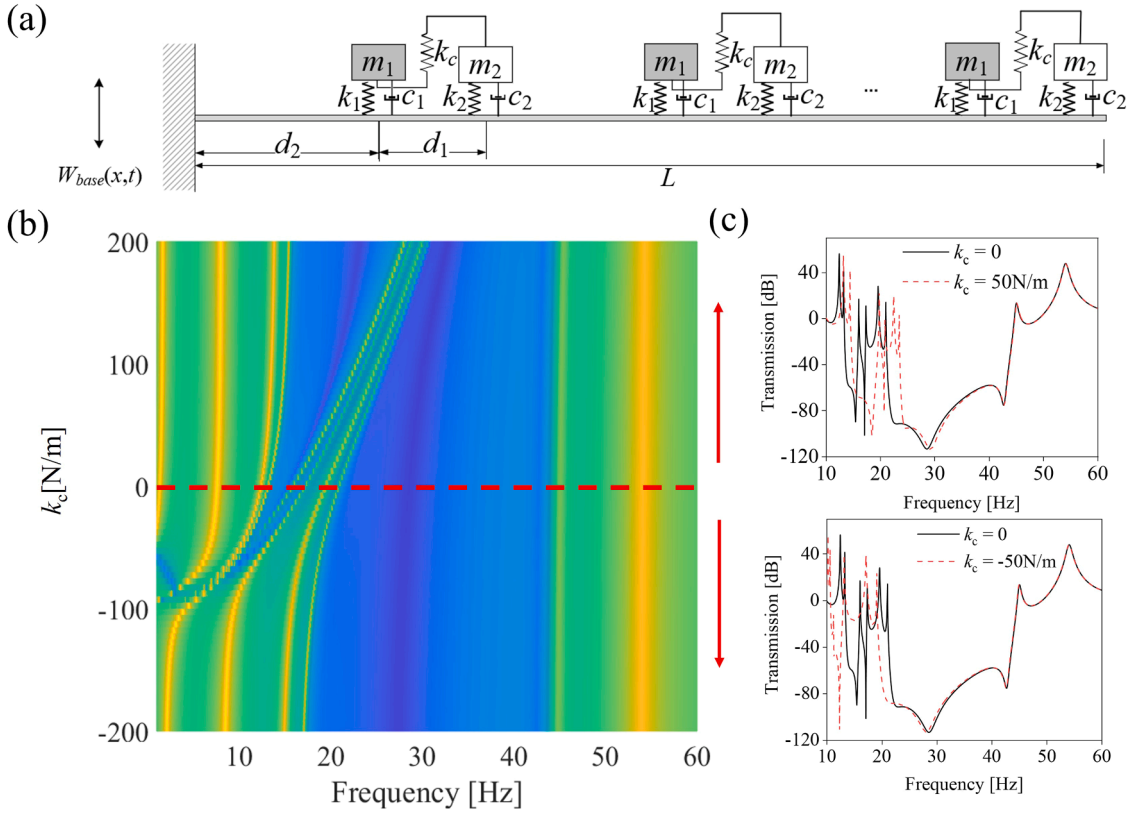

Fig. 6. Linearly coupled metamaterial beam: (a) equivalent model, (b) Effect of coupling stiffness on the transmittance, (c) Transmittance comparison.

two resonators. In such a two-degree-of-freedom internally coupled system—whether in a linear or monostable configuration—the first-order mode is characterized by in-phase motion of the two resonators, while the second-order mode features out-of-phase motion. Since resonator A has a significantly lower natural frequency than resonator B, in the fundamental (in-phase) mode, the vibration response is primarily dominated by resonator A. When the internal coupling stiffness is positive, the in-phase motion leads resonator B to exert an additional inertial force on resonator A, thereby increasing resonator A's reaction force on the host beam and resulting in a broadened bandgap A. Conversely, when the coupling stiffness is negative, resonator B applies a constraint force on resonator A, reducing its effective reaction force on the host beam and thus narrowing bandgap A.

In the second-order (out-of-phase) mode, where resonator B's motion becomes dominant, the effect reverses. A positive coupling stiffness causes resonator A to constrain the motion of resonator B, thereby decreasing its reaction force and narrowing bandgap B. In contrast, a negative coupling stiffness allows resonator A to impart an inertial force onto resonator B due to their opposite phase relationship, enhancing resonator B's reaction force on the host beam and leading to a broader bandgap B.

Therefore, a positive coupling stiffness enhances bandgap A at the expense of bandgap B, while a negative coupling stiffness strengthens bandgap B at the expense of bandgap A, which is the bandgap trade-off phenomenon observed in numerical simulations.

4.3. Nonlinearly coupled configuration

As discussed in the previous section, to achieve large bandgaps at low frequencies, integrating negative stiffness as the internal coupling stiffness is recommended. Therefore, magnetic interaction is introduced to generate the required negative stiffness. The prototype of the nonlinear coupled dual-beam metamaterial is shown in Fig. 7(a). By adjusting the horizontal distance between the tip magnets, the nonlinear force can be controlled, allowing for the study of the effects of nonlinearity strength on the system performance. Fig. 7(b) compares the transmittance of the nonlinear coupled metamaterial with that of its linear counterpart. It is noted that the bandgaps of linear configuration are [13.65, 17.26] Hz and [21.26, 44.40] Hz, respectively. The corresponding bandwidths of bandgap A and bandgap B are 3.61 Hz and 23.14 Hz. After introducing negative stiffness, the two bandgaps shift to be [11.41, 12.31] Hz and [19.46, 44.40] Hz, respectively. The bandwidths of bandgap A and bandgap B changed by −2.71 Hz and 1.80 Hz, respectively, with a clear bandgap enlargement observed in bandgap B.

To further validate the influence of negative stiffness on broadening bandgap B, time-domain responses and the response distribution of the main beam and resonators for both the nonlinearly coupled configuration and its linear configuration are simulated and compared. When subjected to a base excitation (20.40 Hz, 0.1 g), the acceleration at the free end of the linear metamaterial beam was 0.0320 m/s^2, significantly higher than that of the nonlinearly coupled metamaterial beam (0.0018 m/s^2). In terms of response distribution, the linear configuration exhibited large responses with minimal vibration attenuation, whereas the nonlinear configuration

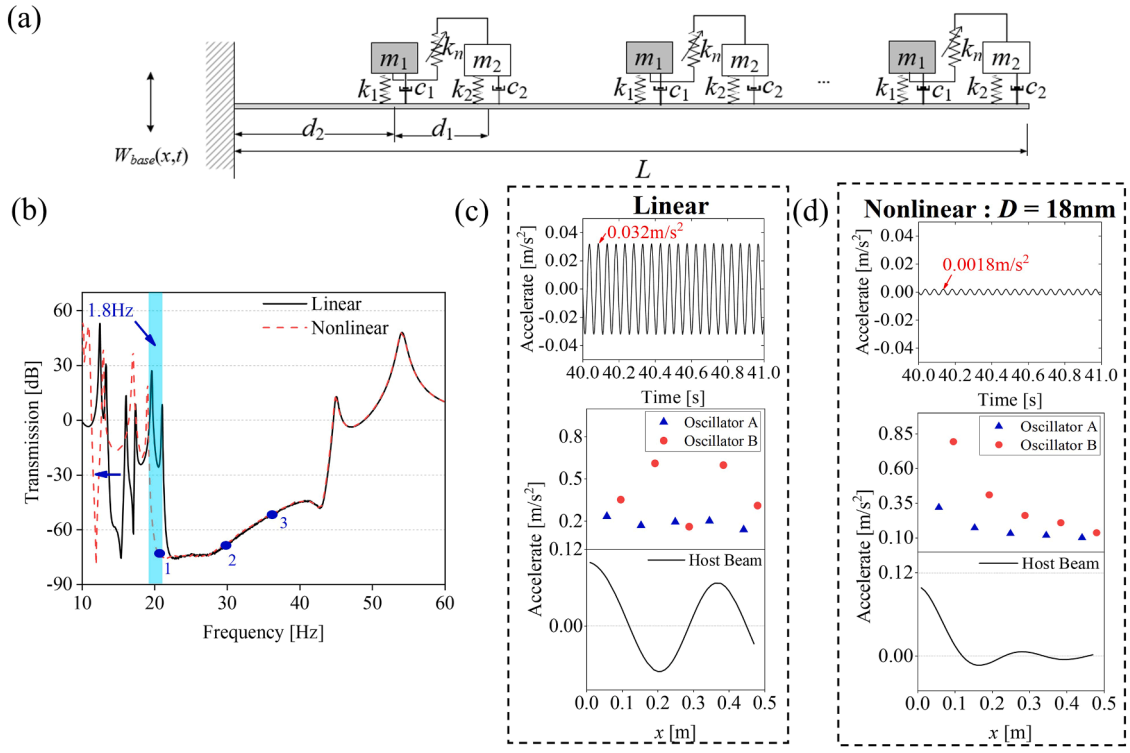

Fig. 7. Nonlinear coupled metamaterial beam: (a) equivalent model, (b) Transmittance comparison between nonlinearly coupled and linear configurations, (c) Response comparison at 20.4 Hz.

showed a rapid reduction in the structural response, indicating pronounced vibration attenuation. Therefore, it is evident that the introduction of negative stiffness transforms the frequency of 20.40 Hz from a point within the passband to a point within the bandgap, representing an effective method to expand the bandwidth.

To investigate the influence of the oscillator number S on the convergence behavior of the method employed in this study, the transmittance responses of both the linear and nonlinear configurations with three different values of S ($S = 6, 8, 10$) are presented in Fig. 1. As shown in Fig. 8(a), as S increases from 6 to 10, the starting and cut-off frequencies of both bandgap A and bandgap B for the linear configuration converge rapidly, and the bandgap structure becomes clearly discernible in the transmittance response at $S = 10$. Similar convergence characteristics are observed in Fig. 8(b) for the nonlinear configuration. Therefore, $S = 10$ is adopted for both configurations in the numerical simulations and experimental investigations.

4.4. *Effect of nonlinearity*

This section mainly focuses on how nonlinearity enlarges the bandgap by gradually decreasing the magnetic distance. Five different magnetic distances were selected: 26 mm, 24 mm, 22 mm, 20 mm, and 18 mm. The transmittance and dynamic responses were obtained and compared in Fig. 9. It is shown that the two bandgaps of the linear configuration are [13.65, 17.26] Hz and [21.26, 44.40] Hz, respectively. After introducing the magnetic interaction, both bandgaps undergo significant changes. For $D = 26$ mm, the two bandgaps are located at [13.05, 16.01] Hz and [20.66, 44.40] Hz, respectively, with the bandwidths of 2.96 Hz and 23.74 Hz, respectively. On one hand, the starting frequencies of both bandgaps move towards lower frequencies. On the other hand, the cut-off frequency of bandgap A decreases, while that of bandgap B remains unchanged. As a result, the width of bandgap A reduced by 0.65 Hz while that of bandgap B increased by 0.60 Hz.

As the magnetic distance decreases, the variation trends of the two bandgaps remain consistent. For bandgap A, both the starting and cut-off frequencies decrease simultaneously, resulting in a narrower bandwidth. In contrast, for bandgap B, while the starting frequency decreases, the cut-off frequency remains unchanged, leading to a widening of the bandwidth. Fig. 9(b) and (c) illustrate how the magnetic distance affects the starting and cut-off frequencies as well as the bandwidth. When the magnetic distance decreases from 26 mm to 18 mm, the starting frequencies of bandgap A are 13.05 Hz, 12.80 Hz, 12.61 Hz, 12.31 Hz, and 11.41 Hz, with corresponding cut-off frequencies of 16.01 Hz, 15.46 Hz, 14.56 Hz, 13.30 Hz, and 12.31 Hz. Both exhibit a clear downward trend, reducing the bandwidth from 3.61 Hz to 0.90 Hz. Meanwhile, the cut-off frequency of bandgap B remains unchanged at 44.40 Hz, while its starting frequency decreases to 20.66 Hz, 20.46 Hz, 20.06 Hz, 19.66 Hz, and 19.46 Hz. Consequently, the bandwidth of bandgap B increases to 23.74 Hz, 23.94 Hz, 24.34 Hz, 24.74 Hz, and 24.94 Hz. Compared to its linear configuration, as the magnetic distance decreases, the bandwidth of bandgap B increased by 0.60 Hz, 0.80 Hz, 1.20 Hz, 1.60 Hz, and 1.80 Hz, corresponding to percentage increases of 2.59 %, 3.46 %, 5.19 %, 6.91 %, and 7.78 %, respectively. This indicates that increasing the nonlinear negative stiffness is an efficient way to enlarge bandgap B. In addition, the total bandgap bandwidth of bandgap A and bandgap B under linear configuration and five magnetic distance is as follows: 26.75 Hz, 26.70 Hz, 26.60 Hz, 26.29 Hz, 25.73 Hz and 25.84 Hz.

In summary, the enhancement of negative stiffness shifts both bandgaps towards lower frequencies. This effect is attributed to the influence of negative stiffness on the resonance frequency of the coupled dual-resonator system, as discussed in Section 3.2. Notably, there is a trade-off between the effects of negative stiffness on bandgap A and bandgap B. While bandgap B widens due to negative stiffness coupling, this comes at the expense of bandgap A. As a result, in terms of overall bandgap performance, introducing nonlinear coupling may not bring any significant advantage. Therefore, the main contribution of internally nonlinear coupling is tuning the bandwidth of bandgap A and bandgap B by utilizing the trade-off performance between these two bandgaps. This trade-off allows the structure to flexibly tune the bandwidth of bandgap A and bandgap B by adjusting the magnetic distance, while the total suppression bandwidth exhibits only minor variation. In practical application, this bandgap trade-off characteristic can be utilized to increase the

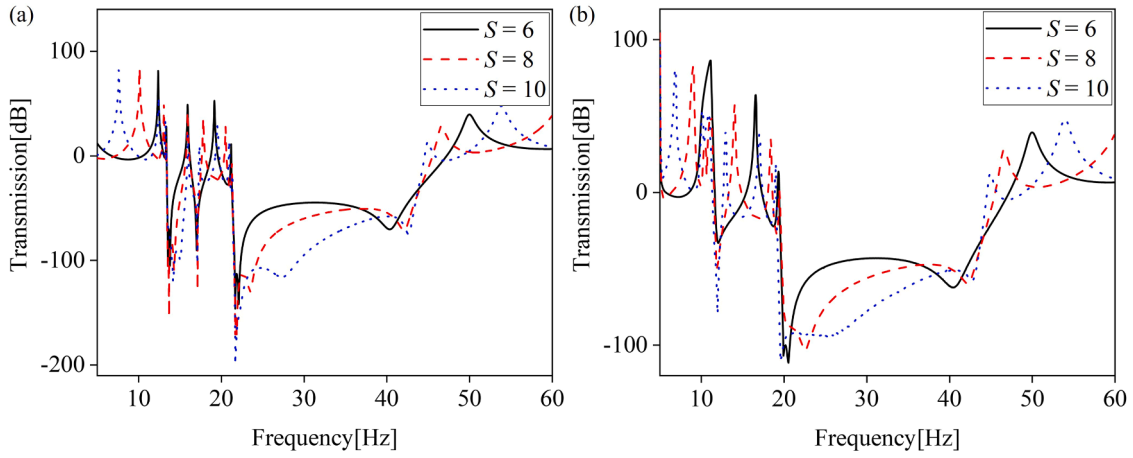

Fig. 8. Effect of oscillator number S on the transmittance response: (a) linear configuration, (b) nonlinear configuration.

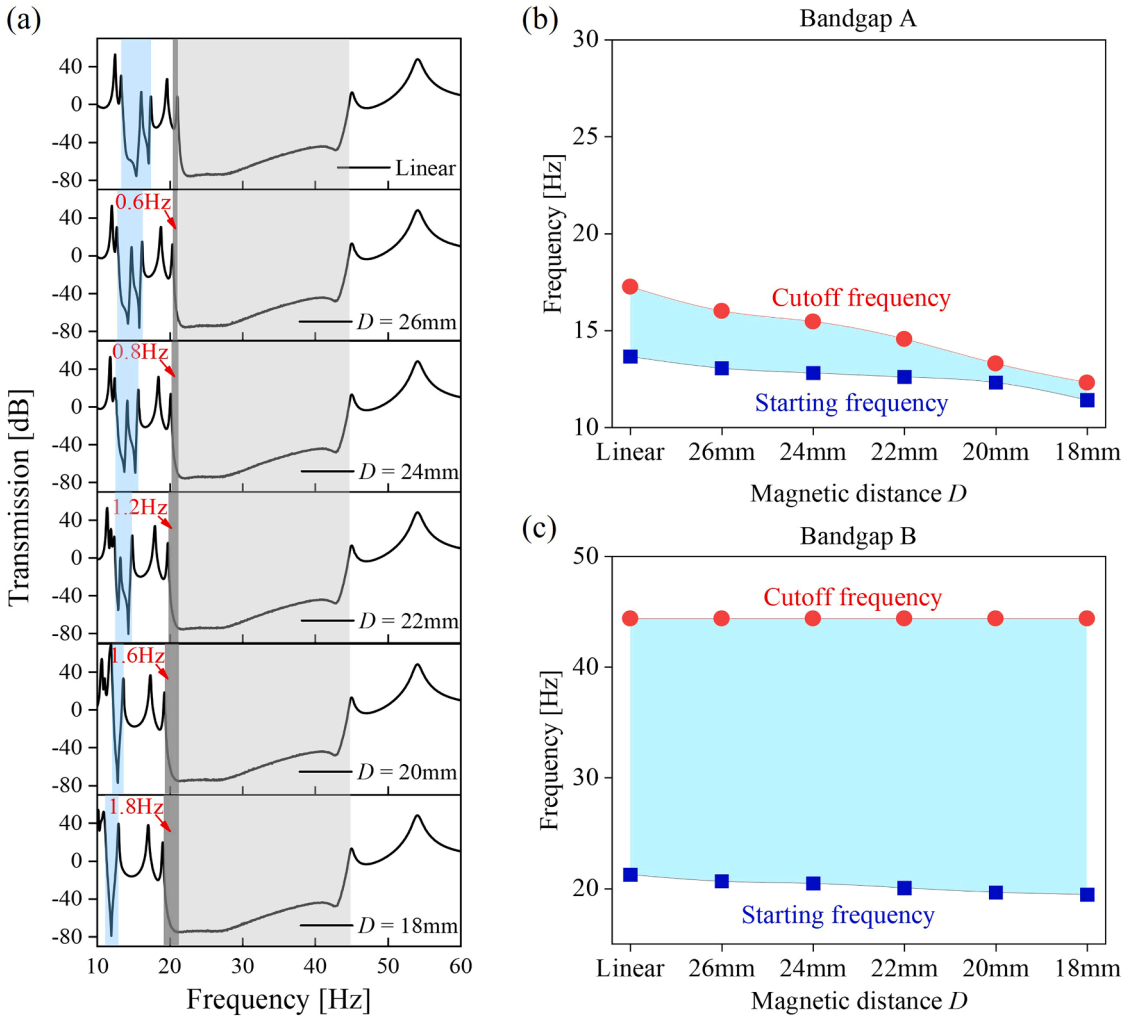

Fig. 9. Effect of magnetic distance: (a) Transmittance, (b) Bandgap A, (c) Bandgap B.

adaptability of the metamaterial under different working conditions.Table 1

Fig. 10 further illustrates the influences of different magnetic distances on the system response at $f = 20.40$ Hz. From the time-domain response, as the magnetic distance decreases from 24 mm to 20 mm and then to 18 mm, the acceleration response at the free end of the metamaterial beam reduces from 0.0170 m/s^2 to 0.0025 m/s^2 and 0.0018 m/s^2, respectively, indicating significant vibration suppression due to the introduction of nonlinear coupling. Meanwhile, the response distributions of the resonators and the main beam are also shown in Fig. 10(b). It is revealed that in both linear and weak nonlinear configurations, the responses are relatively large, with no significant vibration attenuation. As nonlinearity increases, both the resonators and the main beam exhibit pronounced vibration suppression. For instance, for $D = 20$ mm, the main beam's response attenuates from 0.0981 m/s^2 to 0.0025 m/s^2, for $D = 18$ mm, it decreases from 0.0983 m/s^2 to 0.0018 m/s^2, demonstrating significant suppression of main beam vibration.

Notably, while both systems exhibit bandgap characteristics at $D = 18$ mm and $D = 20$ mm, there are differences in the response features of the resonators. At $D = 20$ mm, the response of resonator B is significantly larger than that of resonator A. In contrast, at $D = 18$ mm, the response difference between the two resonators reduces, with the overall response being lower than at $D = 20$ mm. This

Table 1
Numerical simulation results of bandgap B.

	Liner Config.	Nonlinear Config.				
D [mm]	/	26	24	22	20	18
Start frequency [Hz]	21.26	20.66	20.46	20.06	19.66	19.46
Cut-off frequency [Hz]	44.40	44.40	44.40	44.40	44.40	44.40
Bandwidth [Hz]	23.14	23.74	23.94	24.34	24.74	24.94
Increased ratio [%]	/	2.59	3.46	5.19	6.91	7.78

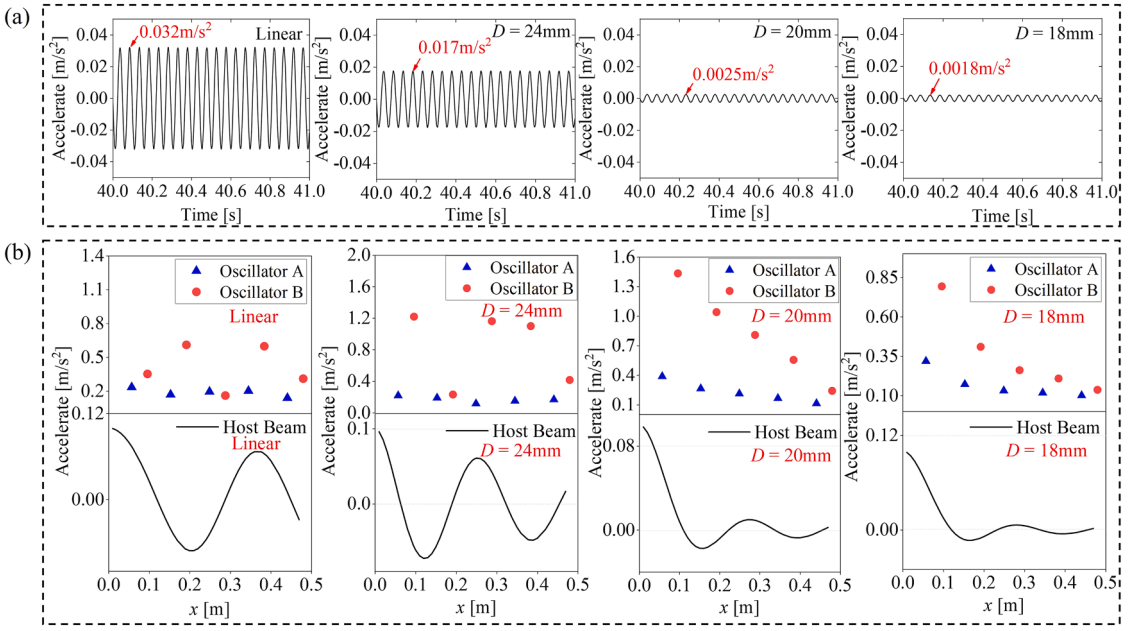

Fig. 10. Effect of magnetic distance on the structural responses at $f = 20.4$ Hz: (a) time-history of acceleration response at free end, (b) response distributions.

difference suggests that in the newly formed bandgap, both resonators A and B contribute effectively to vibration suppression, which plays a key role in the formation of this new bandgap. Unlike in linear metamaterial beams, where only certain resonators contribute to a specific bandgap, all resonators are engaged in generating the new bandgap, resulting in enhanced vibration suppression.

4.5. *Effect of base acceleration*

This section investigates the influence of base acceleration on the bandgap characteristics of a nonlinear metamaterial beam. Five distinct acceleration levels—0.1 m/s², 0.2 m/s², 0.5 m/s², 1.0 m/s², and 2.0 m/s²—are selected for analysis, with the magnetic distance consistently maintained at 18 mm. The transmittance responses of the proposed nonlinear metamaterial beam under these excitation conditions are numerically obtained and comparatively analyzed, as illustrated in Fig. 11. It is clearly observed that as the base acceleration increases from 0.1 m/s² to 2.0 m/s², the bandwidth of the lower bandgap (bandgap A) decreases sharply and nearly vanishes at a base acceleration of 2.0 m/s². The minimum transmittance within bandgap A under increasing base accelerations are –60 dB, –30 dB, –22 dB, –4 dB, and 0 dB, respectively. This phenomenon has been widely reported in nonlinear metamaterial chains and is commonly referred to as an excitation-dependent bandgap [13]. The primary cause of this behavior lies in the cubic coupling stiffness, which effectively narrows the bandwidth of bandgap A under high base accelerations. Meanwhile, it is noteworthy that the influence of

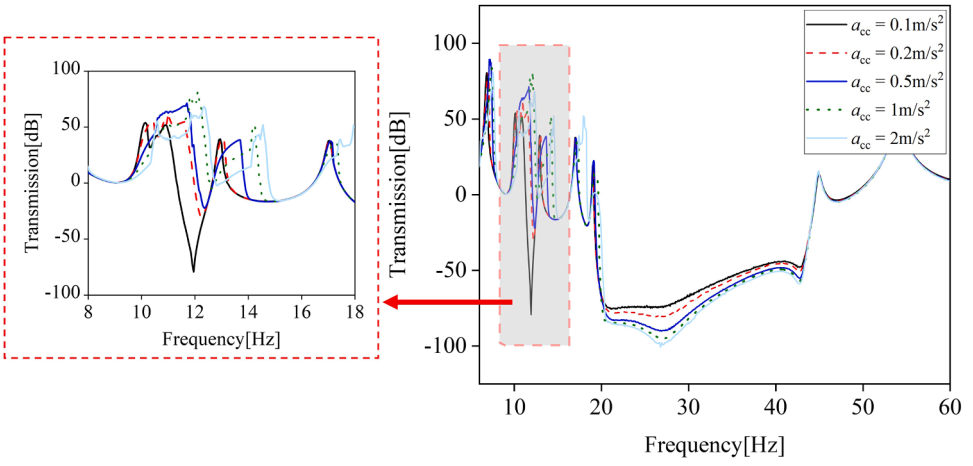

Fig. 11. Effect of base acceleration on the transmittance response.

base acceleration on bandgap B is significantly weaker compared to that on bandgap A (as shown in Table 2). As the base acceleration increases, the starting frequency of bandgap B exhibits a slight upward trend, while its ending frequency remains almost unchanged. Furthermore, the minimum transmittance values within bandgap B under the same acceleration levels are –75 dB, –84 dB, –93 dB, –98 dB, and –102 dB, respectively, indicating that the vibration suppression capability within the second bandgap is well preserved.

Fig. 12 further compares the free-end responses of the metamaterial beam at $f = 12$ Hz (within the center of bandgap A) and $f = 20$ Hz (near the starting frequency of bandgap B) under different base accelerations. As the base acceleration increases from 0.1 m/s^2 to 0.5 m/s^2 and 2.0 m/s^2, the acceleration response at 12 Hz is 0.0025 m/s^2, 1.40 m/s^2, and 30.0 m/s^2, respectively, indicating that $f = 12$ Hz lies within bandgap A under small accelerations but transitions into a passband under large accelerations. Meanwhile, the response at 20 Hz under these three acceleration levels is 0.0047 m/s^2, 0.021 m/s^2, and 0.6 m/s^2, respectively, indicating that the bandwidth of bandgap B is only weakly influenced by increasing base acceleration.

A plausible explanation for the differing effects of base acceleration on these two bandgaps lies in the frequency-dependent nature of nonlinear coupling. According to the governing equation, it is known that the nonlinear term exhibits a cubic dependence on the relative displacement response of the local resonators. Under a given base acceleration, as the excitation frequency increases, the displacement response of the local resonators gradually decreases. Since the relative displacement is less than unity, its cube further reduces the magnitude of the nonlinear term with increasing frequency. Consequently, as the amplitude of the displacement response diminishes, the influence of stiffness nonlinearity on bandgap performance rapidly weakens. Therefore, in this nonlinear magnetically coupled metamaterial, the effect of nonlinear coupling is predominantly confined to the low-frequency bandgap, exerting relatively limited influence on the high-frequency bandgap.

5. Experimental validation

5.1. Experimental setups and parameters identification

To validate the theoretical and simulation results, a nonlinear magnetically coupled metamaterial beam was prototyped and experimentally tested. Fig. 13(a) illustrates the experimental setup of the nonlinear magnetic-coupled beam. The main structure consists of a uniform stainless-steel beam, with dimensions of 480 mm in length, 20 mm in width, and 1 mm in thickness. The main beam is divided into 5 identical unit cells, each containing two pairs of cantilever beam oscillators symmetrically positioned relative to the main beam. Each unit cell has a length of 96 mm, with the cantilever beam oscillators positioned at 57 mm and 39 mm along the unit cell. The cantilever beam oscillators are integrally formed with the main beam and have dimensions of 50 mm in length, 3 mm in width, and 1 mm in thickness. At the free end of each cantilever beam, there is an interface for attaching masses, consisting of 3D-printed mass blocks and aluminum blocks. The 3D-printed mass blocks serve as the tip masses of resonators and can be adjusted by varying the weight of the aluminum blocks embedded, thereby tuning the resonant frequency of the cantilever beam oscillators and the bandgap of the metamaterial beam. Additionally, the 3D-printed mass blocks are equipped with adjustable bolts for installing magnets. By rotating these bolts, the magnetic distance between the coupled beams can be adjusted, thus controlling the magnitude of the nonlinear magnetic force. This setup facilitates the investigation of how nonlinear magnetic forces influence the bandgaps of the metamaterial beam.

Fig. 13(b) presents the vibration test system, which comprises a shaker (DH40020), a power amplifier (DH5872), a controller (VT-9002), an accelerometer (B02BM6), a data acquisition system (DH5922D), and a computer. The vibration controller effectively controlled the output excitation of the shaker, thereby enhancing the accuracy of the tests. Four vibration tests were performed: free damping test, frequency sweep test, single-frequency test and random vibration test. The free damping test is used to identify the structural parameters of the cantilever beam oscillators, including resonant frequency, damping ratio, and equivalent stiffness. The frequency sweep test is to quickly obtain the transmittance profile, and the single-frequency test is to validate the dynamic response under harmonic excitation. The random vibration test is to evaluate the bandgap performance under broadband excitation. The setup for obtaining the transmittance response is illustrated in Fig. 13(c). An acceleration sensor was mounted on the vibration table to measure the input acceleration, while a small, lightweight accelerometer (weighing 2 g) was attached to the test point on the main beam to measure the output acceleration. To avoid potential interference, the accelerometer was not placed on the tip mass of the

Table 2
Effect of base acceleration on bandgaps with $D = 18$ mm.

	Base Acc. [m/s^2]	Start freq. [Hz]	Cut-off freq. [Hz]	Bandwidth [Hz]	Minimum Transmittance [dB]
Bandgap A	0.1	11.28	12.63	1.35	–60
	0.2	11.98	12.63	0.65	–30
	0.5	12.10	12.63	0.53	–22
	1.0	12.58	12.72	0.14	–4
	2.0	12.95	13.02	0.07	0
Bandgap B	0.1	19.14	44.63	25.49	–75
	0.2	19.14	44.63	25.49	–84
	0.5	19.20	44.63	25.43	–93
	1.0	19.43	44.63	25.20	–98
	2.0	19.48	44.63	25.15	–102

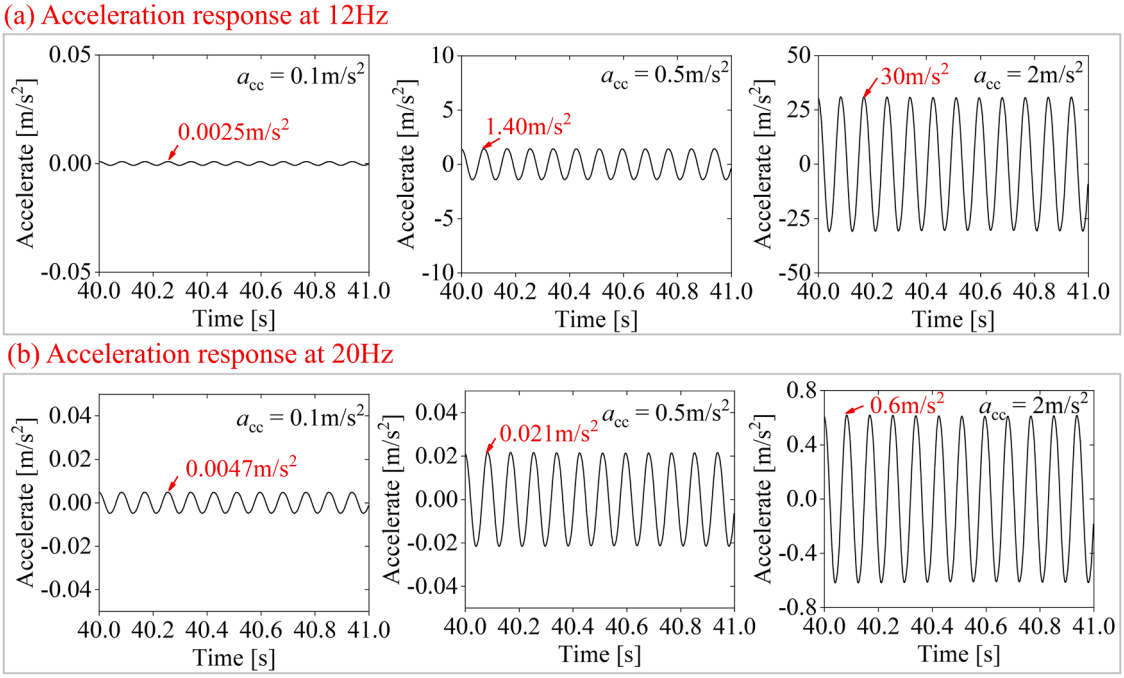

Fig. 12. Effect of base acceleration on the structural responses at $f = 12$ Hz and $f = 20$ Hz: (a) time-history of acceleration response at 12 Hz, (b) time-history of acceleration response at 20 Hz.

resonators. Therefore, the response distribution of the local resonators was not covered by this experiment. First of all, the free damping test of the linear configuration (where the magnets were replaced by the equivalent mass blocks) was conducted, and the identified structural parameters are listed on Table 3

Subsequently, to accurately figure out the relationship between the magnetic force and magnetic distance, magnetic force tests were conducted using a microcomputer-controlled electronic universal testing machine (TSE105D) equipped with a force sensor (BAB-20MT, 0~200 N). N38 neodymium iron boron magnets with a cross-sectional radius of 8 mm and a height of 4 mm were used in the experiments. During the tests, one magnet was fixed to the testing device via an aluminum plate, while the other was attached to a fixed plate, as illustrated in Fig. 14. During the experiment, the horizontal distance D between the two magnets was kept constant, while the vertical distance was varied from +50 mm to −50 mm, allowing for the measurement of the magnetic force at a given D. The experiments were conducted for different D, ranging from 12 mm to 30 mm in increments of 2 mm. Using the identified relationship between magnetic force and magnetic distance, corresponding equivalent stiffness induced by magnetic interaction can be calculated through differential analysis.

Fig. 15(a) shows the force-displacement relationship between the coupled magnets when the magnetic distance D is set to 14 mm. As the vertical displacement x increases from −40 mm to −10 mm, the magnetic force gradually increases and reaches a peak value of 0.631 N at $x = -10$ mm. As x continues to increase beyond −10 mm, the magnetic force starts to decrease, reaching its minimum value of −0.515 N at $x = 10$ mm. This decrease in force with increasing displacement is a characteristic of negative stiffness. As x further increases, the magnetic force rises again. The equivalent stiffness curve in Fig. 15(b) indicates that the coupled magnets exhibit pronounced negative stiffness characteristics within the range of x from −10 mm to 10 mm, with the maximum negative stiffness amplitude of −84 N/m occurring at $x = 0$.

Subsequently, the effects of the magnetic distance D on both the magnetic force and equivalent stiffness are tested. Fig. 15(c) and (d) show that as D decreases, both the nonlinear magnetic force and negative stiffness increase. For example, when $D = 20$ mm, the magnetic force peak is 0.199 N, corresponding to a maximum negative stiffness of −29 N/m. When $D = 26$ mm, the peak magnetic force decreases to 0.070 N, with a maximum negative stiffness of −10 N/m. Finally, based on experimentally measured magnetic forces, a correction coefficient was determined to refine the theoretical magnetic force model. Notably, the equivalent stiffness values for the two cantilever beam oscillators in the unit cell are 181.8 N/m and 256.8 N/m, respectively. This suggests that, under the influence of the coupling magnetic force, the resonant frequencies and bandgaps of the entire system will experience significant changes.

5.2. *Transmittance and dynamic response*

5.2.1. *Linear configuration*

The tests conducted on the linear metamaterial beam include frequency sweep and single-frequency vibration experiments. In the

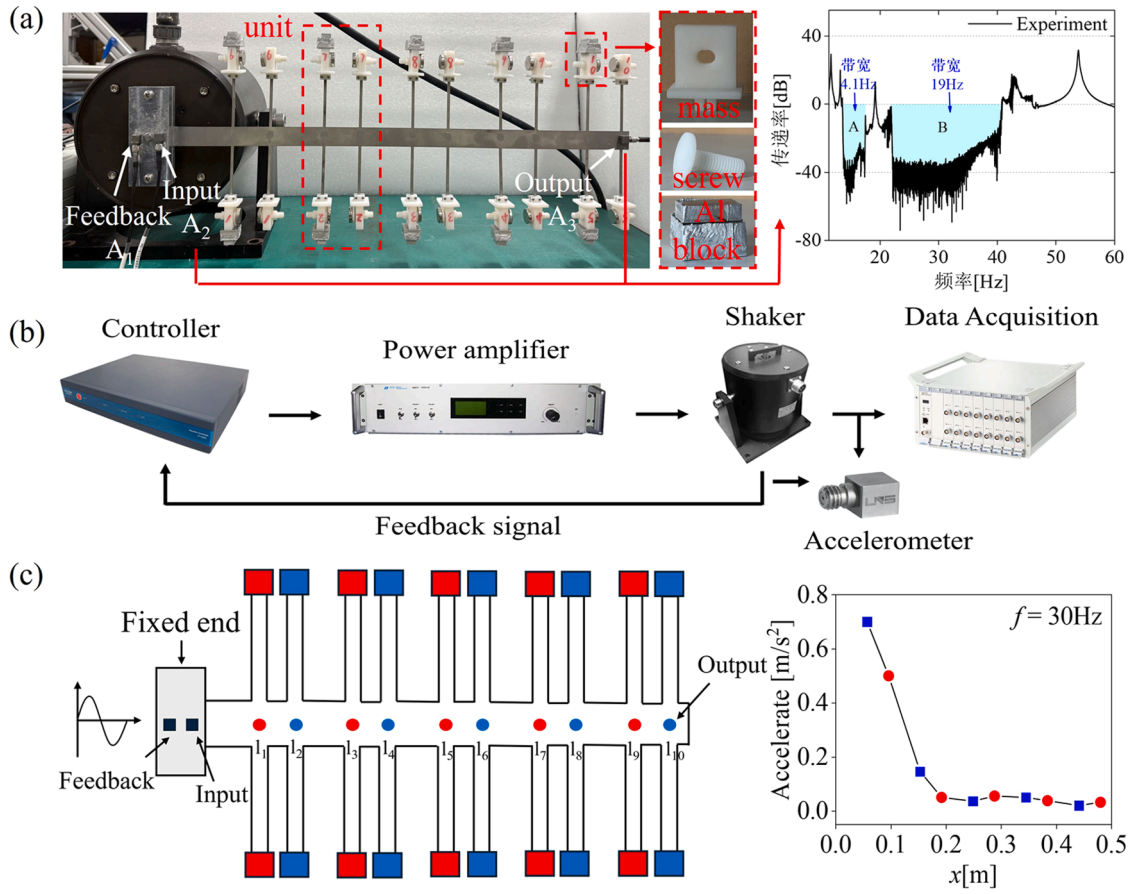

Fig. 13. Experimental setups: (1) nonlinear coupled metamaterial beam, (b) vibration tests systems, (c) method of measuring the transmittance and response distributions.

Table 3
Structural parameters of the cantilever beam oscillators.

Parameter	Value	Parameter	Value
Equivalent mass, m_1 [g]	25.3	Equivalent mass, m_2 [g]	13.8
Equivalent damping coefficient, c_1 [N·m/s]	1.883×10^{-4}	Equivalent damping coefficient, c_2 [N·m/s]	1.169×10^{-4}
Equivalent stiffness, k_1 [N/m]	181.8	Equivalent stiffness, k_2 [N/m]	256.8
Damping ratio, ξ_1	3.213×10^{-4}	Damping ratio, ξ_2	3.1×10^{-5}
Beam length, L [m]	0.48	Beam width, b [m]	0.02
Beam thickness, h [m]	0.001	Beam density, ρ [kg/m^3]	7860
Beam Young's modulus, E	200×10^9	Number of oscillators, S	10
Distance of unit cell, d_1 [mm]	57	Distance of resonators, d_2 [mm]	39

frequency sweep experiment, the linear sweep range was from 10 Hz to 60 Hz, with a sweep rate of 6 Hz/min and an acceleration excitation amplitude of 0.1 g. Fig. 16 compares the simulation and experimentally obtained transmittances of the linear metamaterial beam. The experimental results reveal that the beam exhibits two distinct LR bandgaps: bandgap A in the frequency range of 13.50 Hz to 17.60 Hz, and bandgap B in the range of 21.8 Hz to 40.8 Hz. Within bandgap A, the transmittance varies between −27 dB and −40 dB, while in bandgap B, it ranges from −25 dB to −40 dB. The measured resonant frequencies of cantilever beams A and B are 13.50 Hz and 21.72 Hz, respectively, which correspond precisely to the starting frequencies of bandgaps A and B. This indicates that bandgap A is generated by cantilever beam A, and bandgap B is generated by cantilever beam B, which is consistent with simulation results.

To verify the vibration suppression performance within bandgaps, single-frequency vibration tests were conducted at three frequency points: Point A (15.0 Hz) inside bandgap A, Point B (19.2 Hz) within the passband between bandgaps A and B, and Point C (30.0 Hz) inside bandgap B. During these experiments, a sampling frequency of 2560 Hz and an excitation acceleration of 0.1 g were used. Fig. 17(a) and (b) show that the acceleration response at Point B reached 2.300 m/s^2, significantly higher than those at Points A and C (0.022 m/s^2 and 0.032 m/s^2, respectively). The response distribution of the main beam (Fig. 17(c)) reveals excellent vibration

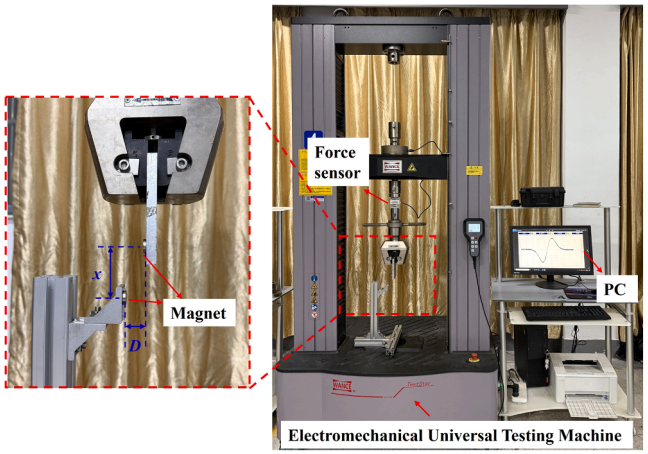

Fig. 14. Experimental setup for magnetic force testing.

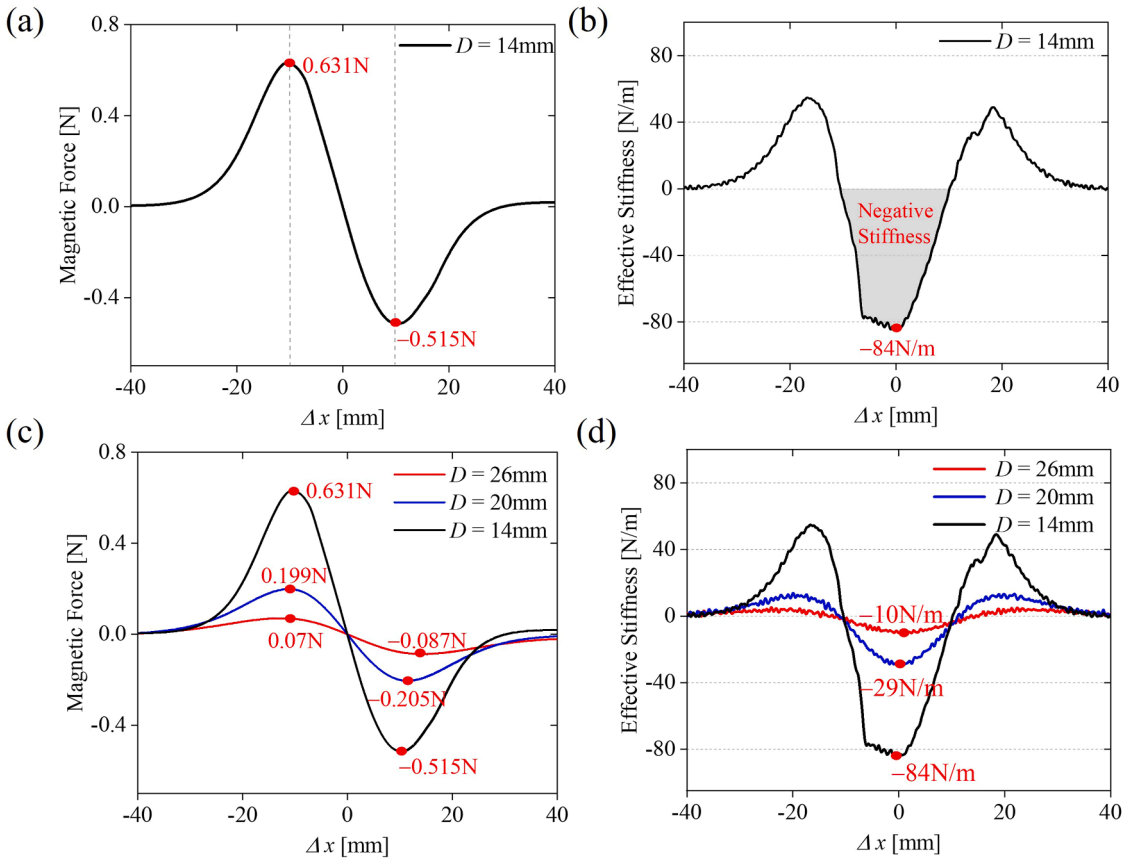

Fig. 15. Experimental results of magnetic force for different D: (a) magnetic force, $D = 14$ mm, (b) equivalent stiffness, $D = 14$ mm, (c) magnetic force, $D = 14$, 20, 26 mm, (b) equivalent stiffness, $D = 14$, 20, 26 mm.

attenuation performance in both the two bandgaps

Further comparisons of the simulation and experimental results reveal that they agree well with each other, although some discrepancies still exist. In bandgap A, a significant peak is observed in the simulation, while the experimental peak amplitude is noticeably lower. In bandgap B, the simulated bandgap is marginally wider than the experimental one, and the vibration transmittance within this bandgap is notably lower in the simulation. These discrepancies can be attributed to two factors: First, due to the manufacturing and assembly accuracy, slight variations between local resonators lead to a narrower bandgap and reduced vibration

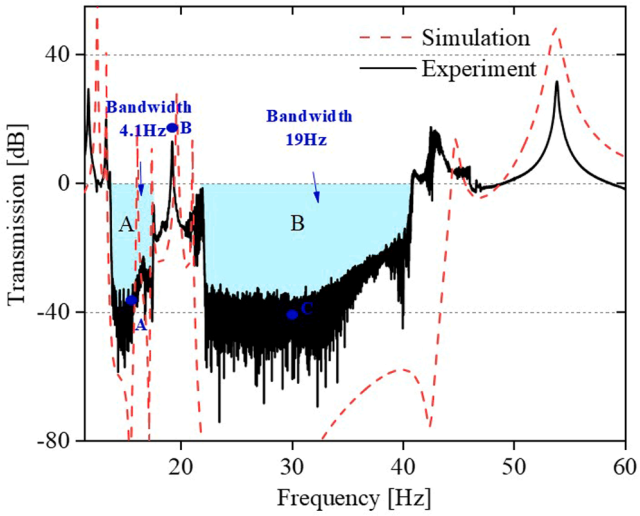

Fig. 16. Comparison between the analytical and experimental transmittance of the uncoupled linear metamaterial beam.

suppression performance. Second, the limitations in the precision of the used accelerometer (0.001 g) restrict the maximum measurable transmittance to −40 dB, which prevents the accurate measurement of lower vibration responses within the bandgap. Despite these discrepancies, the experimental results effectively validate the transmittance and bandgap characteristics of the linear metamaterial.

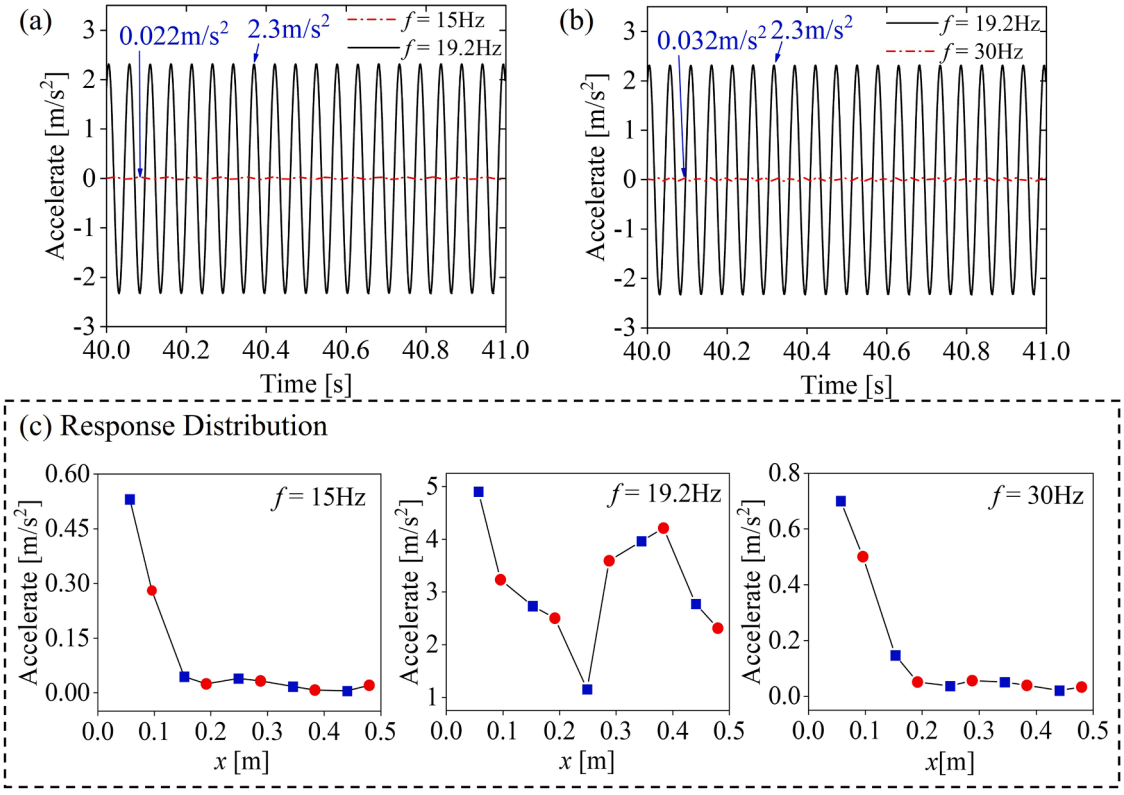

Fig. 17. Dynamic response and response distributions of an uncoupled metamaterial beam: (a) and (b) are the time-history acceleration of the free end of the main beam, (c) the main beam distributions.

5.2.2. Nonlinear configuration

To obtain the dynamic response of the nonlinearly coupled metamaterial beam, frequency sweep and single-frequency vibration tests were conducted with a magnetic distance of $D = 22$ mm. Fig. 18(a) compares the transmittance of the nonlinear coupled configuration with that of the uncoupled linear configuration. For linear configuration, two bandgaps are: 13.50 Hz to 17.60 Hz (4.10 Hz width) and 21.80 Hz to 40.80 Hz (19.00 Hz width). For nonlinear configuration, the two bandgaps shift to: 12.75 Hz to 15.65 Hz (2.90 Hz width) and 20.80 Hz to 40.80 Hz (20.00 Hz width). The introduction of magnetic coupling force resulted in a downward shift in both the starting and cut-off frequencies of bandgap A, decreasing from 13.50 Hz to 12.75 Hz and from 17.60 Hz to 15.65 Hz, respectively, narrowing the bandgap by 29.30 %. For bandgap B, the starting frequency shifted from 21.80 Hz to 20.80 Hz, while the cut-off frequency remained unchanged at 40.80 Hz. Consequently, the width of bandgap A decreased by 1.20 Hz, whereas that of bandgap B increased by 1.00 Hz. These results align well with the findings obtained from numerical simulations (Fig. 7), confirming that the negative stiffness coupling can enlarge bandgap B at the expense of narrowing bandgap A.

To further validate the broadening of bandgap B, single-frequency response tests were conducted on both the uncoupled linear configuration and the magnetically coupled configuration at $f = 21.50$ Hz. In Fig. 18(b), the acceleration response of the magnetic coupled configuration is 0.0018 m/s^2, significantly lower than the linear metamaterial beam (0.0980 m/s^2). Meanwhile, from the response distributions of these two configurations (Fig. 18(b)), it is clearly found that the linear configuration exhibited large responses without noticeable vibration attenuation, whereas the structural response of the nonlinear one rapidly decreased, demonstrating pronounced vibration attenuation. In other words, the frequency of 21.50 Hz has been transformed from passband into bandgap by the appropriate introduction of nonlinear internal coupling.

In summary, based on the experimental results, it is demonstrated that the introduction of nonlinear coupling not only shifts bandgap B to lower frequencies but also broadens its range, providing a viable approach to achieve wide bandgaps at low frequencies.

5.2.3. Effects of magnet distance

As demonstrated in the previous section, the bandgap of LR metamaterial beams can be effectively tuned by introducing the magnetic interaction with negative stiffness, thereby achieving a wider bandgap at low frequencies. This section aims to verify the influence of nonlinear magnetic coupling on the bandgap characteristics of metamaterial beams. The experimental method and setup remain consistent. The distance between the two magnets in each unit cell is adjusted by rotating screws on 3D-printed mass blocks, with magnetic distances set to 22 mm, 20 mm, 18 mm, and 16 mm.

Reducing the magnetic distance leads to significant changes in the transmittance and bandgap features, as shown in Fig. 19. The uncoupled linear configuration exhibits two bandgaps: 13.50 Hz - 17.60 Hz (4.10 Hz width) and 21.80 Hz - 40.80 Hz (19.00 Hz width). With the addition of nonlinear magnetic coupling at a magnetic distance of $D = 22$ mm, the bandgaps shift to 12.75 Hz - 15.65 Hz (2.90 Hz width) and 20.80 Hz - 40.80 Hz (20.00 Hz width). Bandgap A narrows by 1.20 Hz, while bandgap B widens by 1.00 Hz. Similar trends are observed as the magnetic distance reduces. For $D = 20$ mm, the two bandgaps become 12.30 Hz - 14.70 Hz (2.40 Hz width) and 20.30 Hz - 40.80 Hz (20.50 Hz width). For $D = 18$ mm, bandgap A shifts to11.50 Hz - 13.20 Hz (1.70 Hz width) while bandgap B relocates to 19.80 Hz–40.80 Hz (21.00 Hz width). For $D = 16$ mm, bandgap A further decreases to 11.00 Hz - 11.80 Hz (0.80 Hz width) and bandgap B continues to expand to 19.60 Hz - 40.80 Hz (21.20 Hz width).

Moreover, Fig. 19(b) and (c) further show the experimental results of the effects of magnetic interaction on the starting and cut-off frequencies of both bandgaps, as well as the bandwidth. For bandgap A, both starting and cut-off frequencies decrease with the magnetic distance, resulting in a narrower bandgap. For example, as the magnetic distance decreases from 22 mm to 16 mm, the start frequencies of bandgap A are 12.75 Hz, 12.30 Hz, 11.50 Hz, and 11.00 Hz, with corresponding cut-off frequencies of 15.65 Hz, 14.70 Hz, 13.20 Hz, and 11.80 Hz. Both frequencies show a clear downward trend, reducing the bandwidth from 2.90 Hz to 0.80 Hz. Meanwhile, the cut-off frequency of bandgap B remains unchanged at 40.80 Hz, while its starting frequency decreases to 20.80 Hz, 20.30 Hz, 19.80 Hz, and 19.46 Hz. As a result, the bandwidth of bandgap B increases to 20.00 Hz, 20.50 Hz, 21.00 Hz, and 21.20 Hz. Compared to the linear configuration, as the magnetic distance decreases, the increased bandwidth of bandgap B reaches 1.00 Hz, 1.50 Hz, 2.00 Hz, and 2.20 Hz, corresponding to percentage increases of 5.26 %, 7.89 %, 10.53 %, and 11.58 %, respectively. The specific experimental results of bandgap B are summarized in Table 4. In addition, the total bandgap bandwidth of bandgap A and bandgap B under linear configuration and four magnetic distance is as follows: 23.10 Hz, 22.90 Hz, 22.90 Hz, 22.70 Hz and 22.00 Hz.

In summary, the experimental results have validated the main findings obtained from numerical simulations. It has been shown that introducing nonlinear negative stiffness can effectively tune the bandgaps. For bandgap A, this results in a shift towards low frequencies with a narrower bandwidth. For bandgap B, this leads to an expansion to low frequencies with a wider bandwidth. A clear trade-off between bandgap A and bandgap B is clearly demonstrated. Therefore, it can be concluded that introducing nonlinear negative stiffness coupling is an efficient method to achieve a wide bandgap at low frequencies.

5.2.4. Performance under random excitation

To better understand the performance of the proposed nonlinear metamaterial, random vibration tests were conducted in the revised paper. The frequency band of the random base excitation ranges from 10 Hz to 100 Hz, with the acceleration power spectral density set to 0.0005 g^2/Hz. The acceleration responses at the free end were measured for four different configurations, including the linear configuration and three nonlinear configurations with different magnetic distances ($D = 22$ mm, 20 mm, and 18 mm).

Fig. 20 depicts the transmission and output acceleration of these four configurations under random excitation. For the linear configuration, bandgaps are observed at 13.22 Hz–18.80 Hz (bandgap A) and 21.65 Hz–39.25 Hz (bandgap B), which agree well with the results obtained from frequency-sweep experiments. In the nonlinear configuration, the bandgap shifting behavior—similar to that observed in the frequency-sweep experiment—is also evident. As the magnet distance decreases from 22 mm to 18 mm, bandgap A

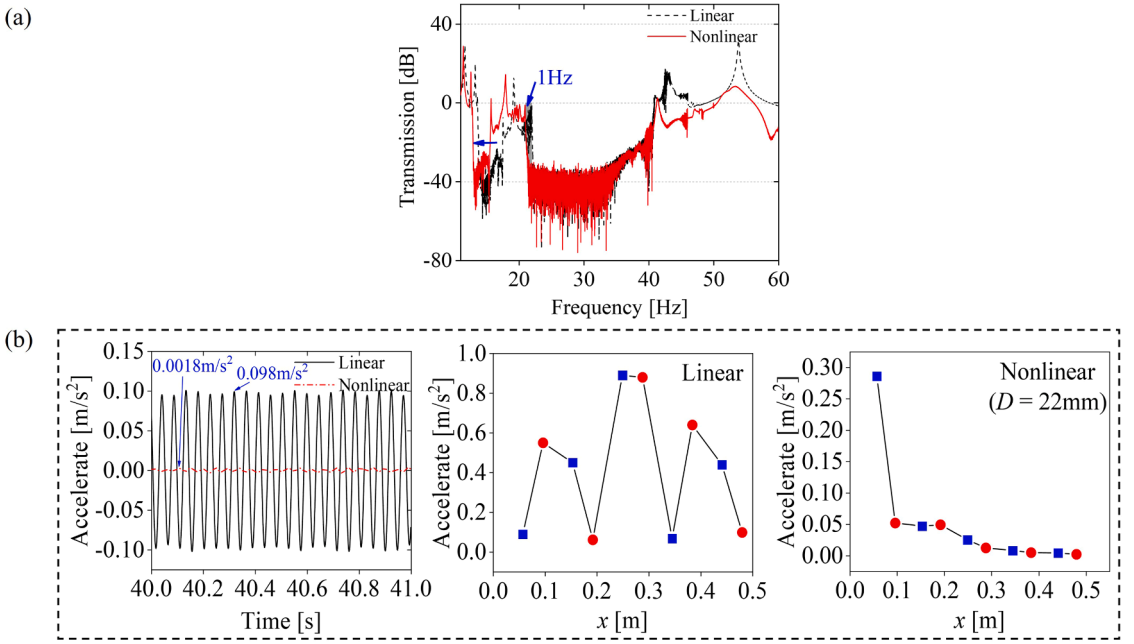

Fig. 18. Experimental results comparison of uncoupled linear configuration and nonlinear coupled configuration (D = 22 mm): (a) transmittance, (b) dynamic response and response distributions at f = 21.5 Hz.

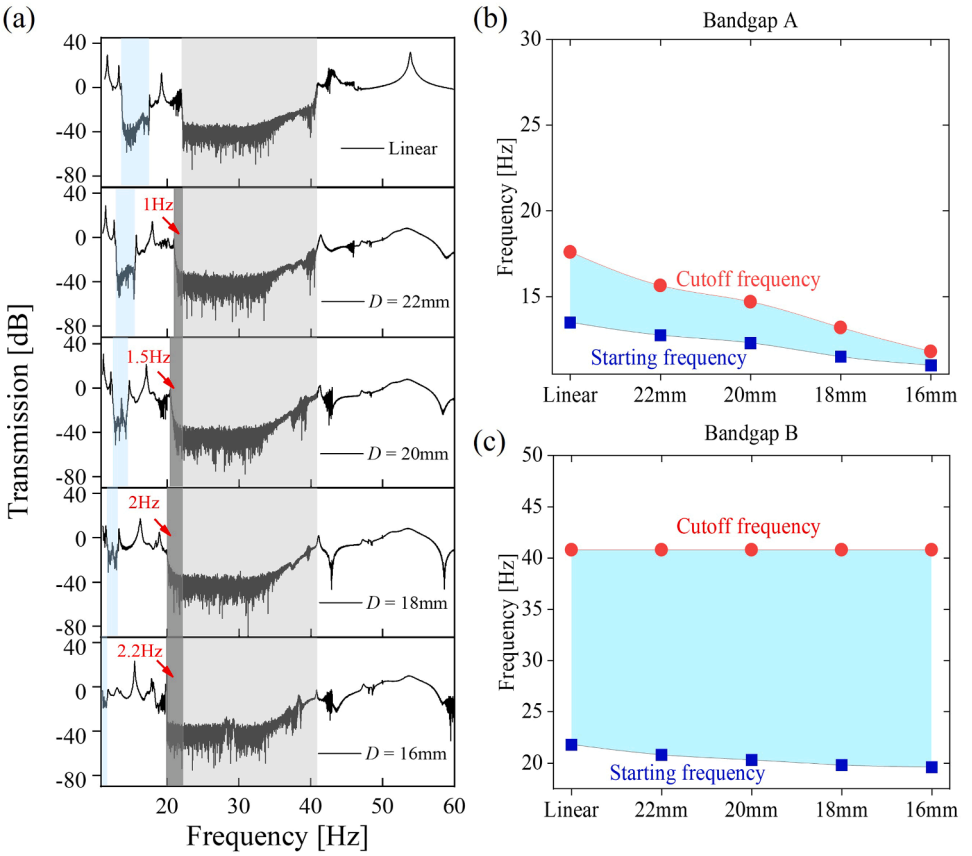

Fig. 19. Experimental results of transmittance for different D:(a) Transmittance, (b) Bandgap A evolution as D varies, (c) Bandgap B evolution as D varies.

Table 4
Experimental results of bandgap B.

	Liner Config.	Nonlinear Config.		
D [mm]	/	22	20	18
Start frequency [Hz]	21.80	20.80	20.30	19.80
Cut-off frequency [Hz]	40.80	40.80	40.80	40.80
Bandwidth [Hz]	19.00	20.00	20.50	21.00
Ratio[%]	/	5.26	7.89	10.53

continuously shifts toward lower frequencies, while bandgap B exhibits an increased bandwidth. For instance, when $D = 22$ mm, bandgap A is located at 12.32 Hz–16.70 Hz with a bandwidth of 4.38 Hz, and bandgap B spans 21.00 Hz–40.40 Hz with a bandwidth of 19.40 Hz. When the magnet distance D is reduced to 18 mm, bandgap A shifts to 11.20 Hz–14.45 Hz with a bandwidth of 3.25 Hz, while bandgap B extends to 20.23 Hz–40.40 Hz with a larger bandwidth of 20.17 Hz. In terms of frequency range and bandwidth, the bandgap performance of this nonlinear metamaterial demonstrates good robustness under both sinusoidal and random excitations. Notably, a minor discrepancy was observed: under random excitation, a small response peak appears within bandgap B. For instance, at $D = 22$ mm, the frequency of this response peak is 32.40 Hz, which is almost two times than one of the resonance peaks in the pass band (11.54 Hz). This small response peak inside bandgap B is mainly due to the high-order harmonics of the resonant peak in the passband, and it does not indicate that the vibration attenuation ability is weakened under random excitation.

6. Conclusions

This paper studied a nonlinear metamaterial beam with magnetically coupled dual-beams as its local resonators. First, the governing equations of the metamaterial beam with magnetic interactions were derived. Subsequently, static analysis was conducted,

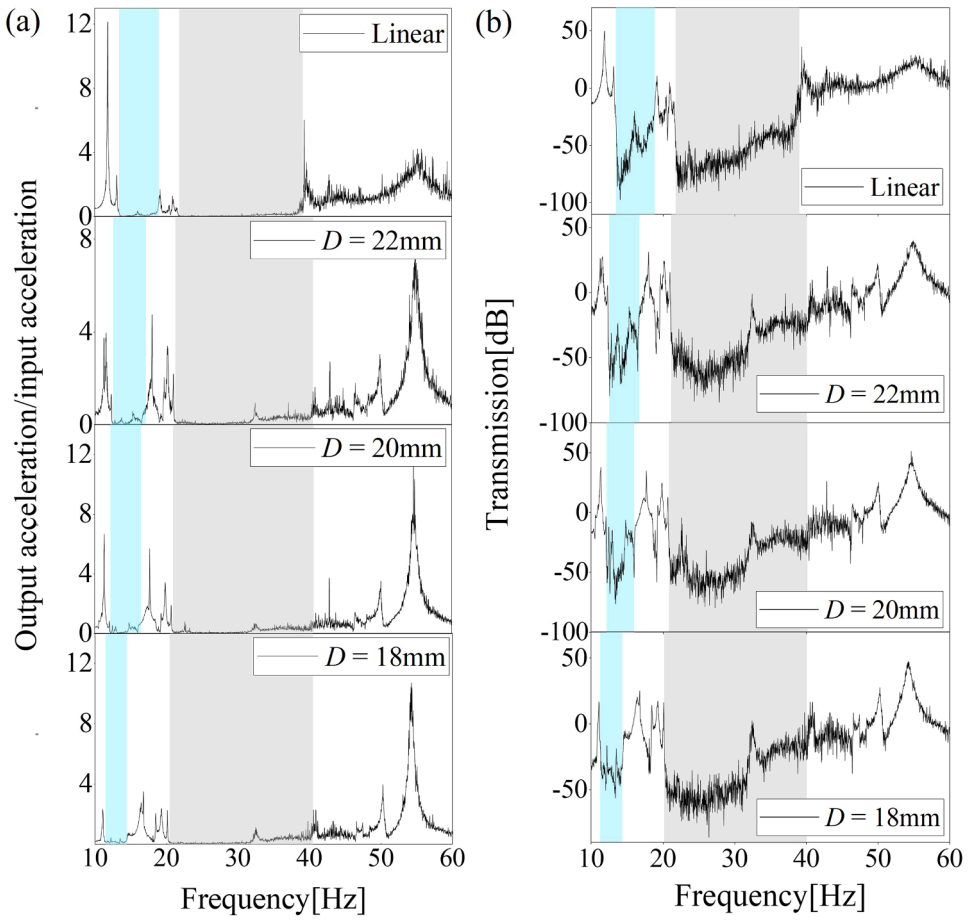

Fig. 20. Influence of different magnetic distances on transmittance under random excitation: (a) output acceleration/input acceleration, (b) transmittance.

focusing on examining magnetic force, equivalent stiffness, and natural frequencies. Following this, both numerical and experimental studies were carried out to study bandgap and dynamic responses of this nonlinear metamaterial. The experimental results were in good agreement with the analytical and numerical results. The key role of nonlinear coupling in shifting the bandgap and enhancing vibration attenuation was identified. Several key conclusions were drawn as follows:

(1) For the internally coupled dual-resonator metamaterial beam, tuning the coupling stiffness induces bandgap trade-off phenomena between the two bandgaps. Under positive stiffness coupling, as the coupling stiffness increases, both bandgaps shift toward higher frequencies, with the bandwidth of the low-frequency bandgap increasing and that of the high-frequency bandgap decreasing. Under negative stiffness coupling, as the coupling strength increases, both bandgaps shift toward lower frequencies, while the bandwidth of the low-frequency bandgap decreases and that of the high-frequency bandgap increases. Meanwhile, the total bandwidth of the two bandgaps exhibits only minor variation. By leveraging this bandgap trade-off characteristic, the position and width of the bandgaps can be flexibly adjusted to match the targeted vibration attenuation requirements.
(2) For the magnetically coupled metamaterial beam, the nonlinear magnetic coupling force incorporates both linear negative stiffness and cubic nonlinear stiffness. This results in an amplitude-dependent bandgap behavior: under small-amplitude excitation, the bandgap location and bandwidth closely match those of its linear counterpart; however, as the excitation amplitude increases, the low-frequency bandgap rapidly narrows and eventually vanishes, whereas the high-frequency bandgap exhibits a slight increase in its starting frequency, with the cut-off frequency remaining nearly unchanged.

In practical applications, the trade-off mechanism of internally-coupled metamaterials enables more efficient and flexible utilization of limited bandgap resources. When the base excitation frequency falls within the low-frequency bandgap, vibration suppression performance can be enhanced by tuning the positive coupling stiffness. Conversely, when the base excitation frequency shifts into the high-frequency bandgap, adjusting the negative coupling stiffness achieves comparable attenuation performance. This strategy of dynamic bandgap allocation and regulation provides a versatile and effective means of mitigating low-frequency multi-line spectrum vibrations as well as variable-frequency vibrations.

CRediT authorship contribution statement

Chunbo Lan: Writing – review & editing, Software, Resources, Conceptualization. **Shuo Wang:** Writing – original draft, Visualization, Validation, Methodology, Investigation, Data curation. **Xi Chen:** Methodology, Investigation, Data curation. **Yang Lu:** Resources, Investigation, Funding acquisition, Conceptualization. **Guobiao Hu:** Writing – review & editing, Supervision, Resources, Project administration, Data curation, Conceptualization.

Declaration of competing interest

I would like to declare on behalf of my co-authors that no conflict of interest exits in the submission of this manuscript, and manuscript is approved by all authors for possible publication. The work described was original research has not been published previously, and not under consideration for publication elsewhere, in whole or in part.

All the authors listed have approved the manuscript that is enclosed.

Acknowledgments

This study was financially supported by the Funds of National Key Laboratory of Helicopter Aeromechanics (grant no. 2024-CXPT-GF-JJ-093-04), the Fundamental Research Funds for the Central Universities (grant no. NT2024002), National Natural Science Foundation of China (grant no. 52305135), Guangzhou Municipal Science and Technology Project (grant no. 2023A03J0011), Guangdong Provincial Key Lab of Integrated Communication, Sensing and Computation for Ubiquitous Internet of Things (grant no. 2023B1212010007), and Guangzhou Municipal Key Laboratory on Future Networked Systems (grant no. 024A03J0623).

Data availability

Data will be made available on request.

References

[1] X. Jiao, J. Zhang, W. Li, Y. Wang, W. Ma, Y. Zhao, Advances in spacecraft micro-vibration suppression methods, Progr. Aerosp. Sci. 138 (2023) 100898.
[2] L. Li, L. Wang, L. Yuan, R. Zheng, Y. Wu, J. Sui, J. Zhong, Micro-vibration suppression methods and key technologies for high-precision space optical instruments, Acta Astronaut. 180 (2021) 417–428.
[3] Z. Liu, X. Zhang, Y. Mao, Y. Zhu, Z. Yang, T. Chan, P. Sheng, Locally resonant sonic materials, Science (1979) 289 (5485) (2000) 1734–1736.
[4] X. Fang, W. Lacarbonara, L. Cheng, Advances in nonlinear acoustic/elastic metamaterials and metastructures, Nonlinear Dyn. 4 (2024) 10219.
[5] O. Alfahmi, C. Sugino, A. Erturk, Duffing-type digitally programmable nonlinear synthetic inductance for piezoelectric structures, Smart Mater. Struct. 31 (2022) 095044.
[6] G. Huang, C. Sun, Band gaps in a multiresonator acoustic metamaterial, ASME-J. Vibrat. Acoust. 132 (2010), 031003-1.

[7] G. Hu, A. Austin, V. Sorokin, L. Tang, Metamaterial beam with graded local resonators for broadband vibration suppression, Mech. Syst. Signal. Process. 146 (2021) 106982.
[8] Z. Miao, J. Yin, Y. Yang, Y. Ke, Z. Zheng, X. Geng, Q. Wang, Design of multi-bandgap metamaterial plate based on composite cylindrical resonators, Mater. Des. 250 (2025) 113570.
[9] K. Yi, M. Collet, Broadening low-frequency bandgaps in locally resonant piezoelectric metamaterials by negative capacitance, J. Sound. Vib. 493 (2021) 115837.
[10] Y. Jian, G. Hu, L. Tang, J. Xu, D. Huang, K. Aw, Graded metamaterial with broadband active controllability for low-frequency vibration suppression, J. Appl. Phys. 136 (2024) 043108.
[11] K. Yi, Z. Liu, R. Zhu, Multi-resonant metamaterials based on self-sensing piezoelectric patches and digital circuits for broadband isolation of elastic wave transmission, Smart Mater. Struct. 31 (2022) 015042.
[12] Y. Jian, G. Hu, L. Tang, W. Tang, M. Abdi, K. Aw, Analytical and experimental study of a metamaterial beam with grading piezoelectric transducers for vibration attenuation band widening, Eng. Struct. 275 (2023) 115091.
[13] X. Fang, J. Wen, B. Bonello, J. Yin, D. Yu, Ultra-low and ultra-broad-band nonlinear acoustic metamaterials, Nat. Commun. 8 (1) (2017) 1288.
[14] Y. Chen, G. Li, R. Sun, G. Chen, Wave dispersion in one-dimensional nonlinear local resonance phononic crystals with perturbation method, Cryst. (Basel) 11 (2021) 774.
[15] Z. Wu, W. Liu, F. Li, C. Zhang, Band-gap property of a novel elastic metamaterial beam with X-shaped local resonators, Mech. Syst. Signal. Process. 134 (2019) 106357.
[16] J. Zhou, K. Wang, D. Xu, H. Ouyang, Multi-low-frequency flexural wave attenuation in Euler–Bernoulli beams using local resonators containing negative-stiffness mechanisms, Phys. Lett. A 381 (2017) 3141–3148.
[17] J. Zhang, J. Zhang, B. Zhang, Y. An, X. Yang, N. Hu, L. Ma, Y. Peng, B. Wang, Broadband multifrequency vibration attenuation of an acoustic metamaterial beam with two-degree-of-freedom nonlinear bistable absorbers, Mech. Syst. Signal. Process. 212 (2024) 111264.
[18] J. Zhou, L. Dou, K. Wang, D. Xu, H. Ouyang, A nonlinear resonator with inertial amplification for very low-frequency flexural wave attenuations in beams, Nonlinear Dyn. 96 (2019) 647–665.
[19] J. Mosquera-Sánchez, Marqui De, C. Jr, Broadband and multimode attenuation in duffing- and NES-type piezoelectric metastructures, Int. J. Mech. Sci. 270 (2024) 109084.
[20] C. Zhang, D. Zhang, F. Yin, M. Guo, F. Ma, C. Wu, Borrow-force-attack-force" by multi-scale elastic metamaterial with nonlinear damping, Compos. Part B 288 (2025) 111884.
[21] X. Fan, X. Mao, Y. Dong, H. Liu, M. Shao, L. Wang, Tunable bandgaps of a metamaterial beam with nonlinear magnetic resonators, Nonlinear Dyn. 112 (2024) 9743–9765.
[22] P. Sheng, X. Fang, J. Wen, D. Yu, Vibration properties and optimized design of a nonlinear acoustic metamaterial beam, J. Sound. Vib. 492 (2021) 115739.
[23] B. Zhao, H. Thomsen, X. Pu, S. Fang, Z. Lai, B. Dammed, A. Bergamini, E. Chatzi, A. Colombi, A nonlinear damped metamaterial: wideband attenuation with nonlinear bandgap and modal dissipation, Mech. Syst. Signal. Process. 208 (2024) 111079.
[24] Z. Guo, G. Hu, V. Sorokin, L. Tang, X. Yang, J. Zhang, Low-frequency flexural wave attenuation in metamaterial sandwich beam with hourglass lattice truss core, Wave Motion 104 (2021) 102750.
[25] X. Xu, M. Barnhart, X. Fang, J. Wen, Y. Chen, G. Huang, A nonlinear dissipative elastic metamaterial for broadband wave mitigation, Int. J. Mech. Sci. 164 (2019) 105159.
[26] M. Fronk, L. Fang, P. Packo, M. Leamy, Elastic wave propagation in weakly nonlinear media and metamaterials: a review of recent developments, Nonlinear Dyn. 111 (2023) 10709–10741.
[27] K. Manktelow, M. Leamy, M. Ruzzene, Multiple scales analysis of wave–wave interactions in a cubically nonlinear monoatomic chain, Nonlinear Dyn. 63 (1) (2011) 193.
[28] V. Zega, P. Silva, M. Geers, V. Kouznetsova, Experimental proof of emergent subharmonic attenuation zones in a nonlinear locally resonant metamaterial, Sci. Rep. 10 (1) (2020) 12041.
[29] B. Deng, P. Wang, Q. He, V. Tournat, K. Bertoldi, Metamaterials with amplitude gaps for elastic solitons, Nat. Commun. 9 (1) (2018) 1.
[30] A. Banerjee, S. Adhikari, M. Hussein, Inertial amplification band-gap generation by coupling a levered mass with a locally resonant mass, Int. J. Mech. Sci. 207 (2021) 106630.
[31] X. Fang, J. Wen, D. Yu, J. Yin, Bridging-coupling band gaps in nonlinear acoustic metamaterials, Phys. Rev. Appl. 10 (2018) 054049.
[32] G. Hu, L. Tang, R. Das, Internally coupled metamaterial beam for simultaneous vibration suppression and low frequency energy harvesting, J. Appl. Phys. 123 (2018) 055107.
[33] G. Hu, L. Tang, J. Xu, C. Lan, R. Das, Metamaterial with local resonators coupled by negative stiffness springs for enhanced vibration suppression, ASME-J. pf Appl. Mech. 86 (2019) 081009.
[34] Y. Xue, J. Li, Y. Wang, F. Li, Broadband vibration attenuation in nonlinear meta-structures with magnet coupling mechanism: theory and experiments, Commun. Nonlinear Sci. Numer. Simulat. 127 (2023) 107543.
[35] K.W. Yung, P.B. Landecker, D.D. Villani, An analytic solution for the force between two magnetic dipoles, Magnet. Electr. Separat. 9 (1998) 39–52.